Energy-efficient Micro-Motor Control for Mobile Robots

Bachelor Thesis 2

in partial fulfillment of the requirements for the degree

"Bachelor of Science in Engineering"

Bachelor program:

Mechatronics - Mechanical Engineering

Management Center Innsbruck

Supervisor:

Mingoo Seok, PhD

Internal supervisor:

Ing. Ronald Stärz

Author:

Andreas Hofmann

1110602008

Declaration in lieu of oath

„I hereby declare, under oath, that this bachelor thesis has been my independent work and has not been aided with any prohibited means. I declare, to the best of my knowledge and belief, that all passages taken from published and unpublished sources or documents have been reproduced whether as original, slightly changed or in thought, have been mentioned as such at the corresponding places of the thesis, by citation, where the extent of the original quotes is indicated.

The paper has not been submitted for evaluation to another examination authority or has been published in this form or another.“

Place, day/month/year

Signature

Acknowledgment

First, I want to thank the Marshall Plan Foundation, which supported me with a scholarship to finance the stay in New York City.

Furthermore, I thank my parents, because they assisted me with further financing and supported me through the whole bachelor degree course.

I want to give very special thanks to Prof. Mingoo Seok, who supervised me and helped me a lot during my work. Without him my research at the Columbia University would not have been possible.

Finally, I want to thank all people I have met in that time and all my friends, who visited me. They have made the stay in New York much more fun.

Kurzfassung

Der Einsatz von mobilen Robotern wird immer wichtiger und deren Anwendung findet immer mehr Verbreitung. Die beschränkte Traglast begrenzt die Anzahl von Energiespeichern besonders für kleine, mobile Roboter und deswegen haben diese eine kurze Betriebszeit. Darum ist die Minimierung des Energieverbrauchs ein wichtiges Anliegen bei der Auslegung von mobilen Robotern. Der Großteil der Energie wird von den Motoren verbraucht. Deshalb führt eine energie-optimale Motorregelung zu signifikanten Energieeinsparungen des mobilen Roboters. Das Ziel ist es, die Position des mobilen Roboters zu regeln und dabei den Energieverbrauch zu minimieren.

Ein bürstenloser Gleichstrommotor (BLDC Motor) wird aufgrund des hohen Wirkungsgrades und der geringen Verluste verwendet. Zuerst werden alle auftretenden Verluste eines BLDC Motors festgelegt. Danach wird ein Modell hergeleitet, das den Zusammenhang zwischen dem Motormoment und der Geschwindigkeit des mobilen Roboters beschreibt. Darauffolgend wird eine energie-optimale Regelung mit Hilfe des linear-quadratischen Reglers (LQR) implementiert. Ein konventioneller Proportional-, Integral-, Differenzier- (PID) Regler wird verwendet, um den Energieverbrauch zu vergleichen.

Ein Simulationsmodell des BLDC Motors und des mobilen Roboters wurde erstellt. Das Modell des BLDC Motors wird durch Aufzeichnung und Vergleich der Leistungskurven aus dem Datenblatt überprüft. Die Position des mobilen Roboters wird geregelt und die Kupferverluste, welche die größten Verluste des BLDC Motors sind, werden durch eine energie-optimale Regelung reduziert. Jedoch haben die Energieeinsparungen auch eine längere Ausregelzeit zur Folge.

Es wird der Schluss gezogen, dass die Betriebszeit von mobilen Robotern durch eine geeignete Motorregelung verlängert werden kann. Dies ist für die zukünftige Anwendung von Bedeutung und dadurch wird der Einsatz verbessert. Zusätzlich kann diese Implementierung der Energieeinsparung auch für andere Robotertypen, wie zum Beispiel für unbemannte Mikro-Luftfahrzeuge, verwendet werden.

Schlagwörter: energie-optimale Regelung, bürstenloser Gleichstrommotor, mobiler Roboter, Energieeffizienz

Abstract

The use of mobile robots becomes more important and their field of applications are currently growing. The payload constraints limit the amount of energy storage especially for small mobile robots and thus, they have a short operational time. Therefore, a critical concern in designing mobile robots is to minimize energy consumption. The majority of energy is consumed by the motors. So, an energy optimal motor control leads to significant energy savings of the mobile robot. The objective is to control the position of the mobile robot by minimizing the energy consumption.

A brushless direct current (BLDC) motor is used, because it has a high efficiency and less wear. First, all occurring losses of a BLDC motor are determined. Then, a model of the relationship between motor torque and the velocity of the mobile robot is deduced. After that, an energy optimal control system based on the linear quadratic regulator (LQR) is implemented. An conventional proportional-, integrative-, derivative (PID) controller is used to compare the energy consumption.

A simulation model of the BLDC motor and the mobile robot motion is created. The BLDC motor model is verified by plotting and comparing the performance diagrams of the data sheet. The position of the mobile robot is controlled and the copper losses, which are the highest losses of a BLDC motor, are reduced due to energy optimal control. However, these energy savings result in a longer settling time.

It is concluded, that the operational time of mobile robots could be prolonged by appropriate control of their motors. This improves its operation and is significant for the applications of mobile robots in future. Furthermore, this implementation of saving energy could be used for other types of robots like the micro unmanned aerial vehicle.

Keywords: energy optimal control, brushless direct current motor, mobile robot, energy efficiency

Contents

1 Introduction

1.1 Motivation

The population of mobile robots has been growing fast in the last few years and they will be an emerging field in the future. They are already used in some applications like vacuum cleaners and lawn mowers. One problem mobile robots have to face is the limited operational time. They are usually energized by a battery which has to be re-charged after some time in operation. The amount of energy storage is limited due to payload constraints especially for small mobile robots. Thus, the minimization of the power consumption is a major concern in designing mobile robots.

The motors of mobile robots are consuming most of the energy. To achieve an energy-efficient mobile robot a permanent magnet brushless direct current (PMBLDC) motor is chosen. This type of motor has no wear caused by brushes, which is a major problem for brushed DC motors. Thus, the BLDC motor is more durable, but provides the good controlability as the brushed type. An appropriate control of the motor leads to significant energy savings of the mobile robot.

1.2 Previous Work

Many work was done about modeling the BLDC motor. Stefán Baldursson [1] presents a BLDC motor model in MATLAB®/SIMULINK®. It is compared to a brushed DC motor model. The motor is controlled by hysteresis band control, pulse width modulation (PWM) control and variable DC link voltage control.

K.Shivanarayana et al. [2] introduce a four quadrant operation and speed control of a BLDC motor using MATLAB®/SIMULINK®. Thus, the electric machine is able to be driven as motor and generator in the model.

Additionally, some work is done about sensorless control of the BLDC motor. Nobuyuki Matsui [3] describes a sensorless method where the position is estimated in a voltage and current model.

P. Damodharan and Krishna Vasudevan [4] implement a novel sensorless control. The position information is achieved by zero-crossing detection of back electromotive force (back EMF) out of the line voltage difference. Many sensorless control techniques are based on the zero-crossing of the back EMF. This back EMF is hard to measure, but substracting the two line voltages provides information about the zero-crossing of the back EMFs. Thus, measuring the line voltage differences is an easier way for position estimation.

F. Klenke et al. [5] describe an energy optimal motion. A comparison between time and energy optimal motion is done and the effect of downsizing components is explained.

1.3 Objective

The aim of this thesis is to minimize energy consumption of a small mobile robot. Therefore, an energy-optimal control should be implemented to regulate the micro BLDC motor. This should be done by minimizing the current and thus, reducing the copper losses. The highest losses in a motor are these copper losses. The motor is modeled in MATLAB®/SIMULINK® and the model is proved by plotting the performance diagrams provided by the data sheet. Afterwards, the dynamics of motion are modeled and the position of the mobile robot is controlled. Energy-optimal control is compared to a proportional-, integrative-, derivative (PID) controller, which is used for time optimal control. The currently smallest BLDC motor is chosen to be controlled, which is the micro BLDC motor DM1422-03 of Telco Motion [6]. The dimensions of this BLDC motor are shown in figure 1.1. The key specifications are

$$\begin{aligned} V_{rate} &= 3V, \\ I_{rate} &= 0.01A, \\ n_{rate} &= 233min^{-1}, \\ T_{rate} &= 0.21mNm, \\ P_{out} &= 0.01W, \\ \eta_{max} &= 0.18, \end{aligned}$$

where

V_{rate} is the rated voltage,
I_{rate} is the rated current,
n_{rate} is the rated rotational speed,
T_{rate} is the rated torque,
P_{out} is the rated mechanical output power,
η_{max} is the maximal efficiency. [6]

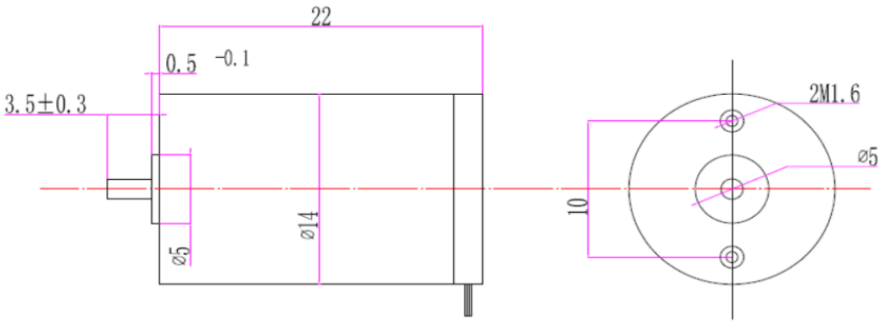

Figure 1.1: Dimensions of the chosen BLDC motor. [6]

1.4 Structure of the Thesis

In chapter 2 the brushless DC motor is explained. This includes the description of the driving principle, the construction, advantages and disadvantages of this motor type. Additionally, the power electronics for the electronically commutation, the so-called inverter, is described. Furthermore, the

theoretical mathematical model is derived as differential equations, transfer functions and state space representation. At last, the losses of this motor are discussed.

In chapter 3.12 the tractive effort force to achieve the desired acceleration of the mobile robot is deduced. All disturbances which acts on the robot are described. Afterwards, a mathematical model is derived to explain the behavior between motor torque and speed of the mobile robot. This includes the differential equations and the transfer function.

Chapter 4 details the control design for time optimal and energy optimal control. This includes the description of a PID controller. The time optimal control is implemented with a PID controller. The optimal control theory is explained, which is used to implement the energy-optimal control.

In chapter 5 the SIMULINK® model of the motor drive is specified. This contains the BLDC motor, inverter and the switch logic. Furthermore, the implementation of the energy optimal controller and the mobile robot behavior is considered in this chapter.

All results are presented in chapter 6. The starting behavior of the motor, the verification of the motor model, the step response of the robot position and the energy savings are included in this chapter.

In chapter 7 a conclusion of the thesis is given.

2 Brushless Direct Current Motor

The brushless direct current motor (BLDC motor) is contrary to its name a special synchronous motor. A direct current source is converted to an alternating current through a power electronics switching circuit, called inverter. Thus, the mechanical commutator of a brushed DC motor is replaced through the inverter. The BLDC motor has the same speed-torque behavior like the brushed dc motor. [1] A very similar motor is the so-called permanent magnet synchronous motor (PMSM). The main difference between the BLDC motor and PMSM is its trapezoidal back electromotive force (back EMF) instead of the sinusoidal back EMF for the PMSM. [7, pp. 48] But some papers refer both trapezoidal and sinusoidal back EMF types as BLDC motor. [1, p. 8]

The BLDC motor has gained much attention for the last two decades due to the improvements in power electronics [8, pp. 3]. The inverter needs a position information of the rotor to generate the right switching sequence. This position is mostly measured by hall sensors. But sensorless techniques are invented to save cost and space. [1] Thus, sensorless control is used for micro motors. There are different methods which are implemented for sensorless control [8, pp. 167-206]. These techniques are described later in this chapter. In this paper, the position is obtained by the integration of the output speed of the BLDC motor model.

2.1 Driving Principle

This section describes a very simplified driving principle of a BLDC motor to achieve an overview and to understand the mode of operation of this kind of motor. Figure 2.1 shows the driving principle in three steps. The components of the BLDC motor are the rotor in the middle and the stator, which is connected to the inverter switching circuit at the bottom. In Figure 2.1 a) the current through the inverter generates a north and south pole at the stator and the rotor is attracted clockwise. Before the rotor and stator poles are in equilibrium like in figure 2.1 b) the inverter switches are opened. The rotor is not attracted anymore and the momentum causes it to move further. Beyond this point, the inverter commutates the current and changes the stator poles to the opposite direction which can be seen in figure 2.1 c). Thus, the rotor is attracted again. To improve the efficiency of the BLDC motor the stator can be made out of three coils and the rotor of two or more pole pairs. Thus, a three phase inverter is needed to commutate the three stator currents. The figure also shows that the inverter needs a position information to commutate the current at the right time. This is explained later in this chapter. [9, pp. 167-169]

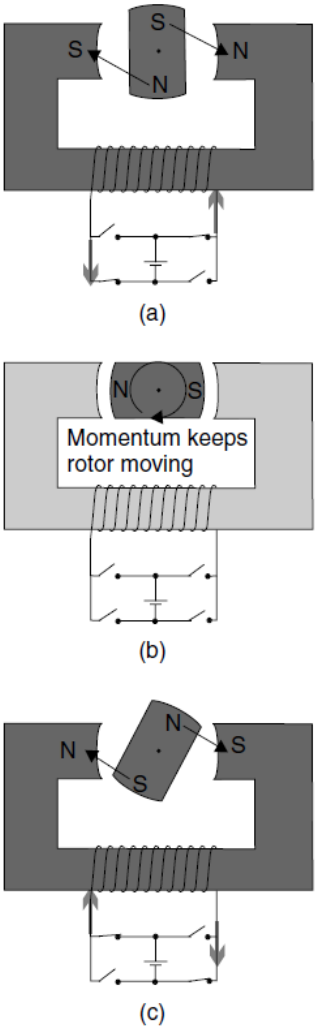

Figure 2.1: Simplified driving principle of a BLDC motor. [9, p. 168]

2.2 Construction

Figure 2.2 shows the cross-section of a four pole BLDC motor with three coils. The motor consists of a rotor, a stator and position sensors and the whole drive system includes the motor, inverter and a switching logic block. The logic block needs position information to generate the right switching sequences for the inverter. Therefore, position sensors or sensorless techniques are applied. The most common position sensors are hall sensors because of its low cost and simplicity. [8, pp. 25-28]

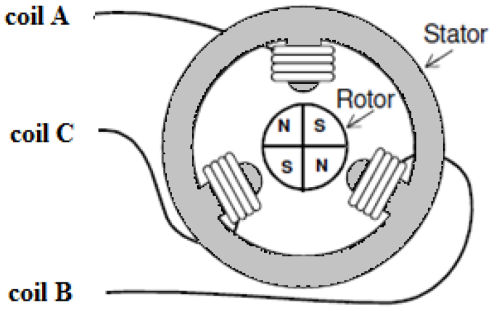

Figure 2.2: cross-section of a BLDC motor. [10]

The whole drive scheme of a BLDC motor can be seen in figure 2.3. This motor consists of three stator windings *U, W and V* and three hall sensors *HA, HB and HC* which are mounted on the stator with an orientation of 120° to each other. Each stator winding consists of two coils, which regard as opposing poles if current is flowing. The rotor is a two pole permanent magnet. Three phase star-connected BLDC motor are the most common types due to better performance and lower cost [8, pp. 26-27]. The star point is marked with *S*. On the top is the switching circuit, which is a three phase full-bridge inverter. The switching sequence is generated by a logic block, which has the hall sensor signals as inputs. The connections between logic block and power transistor gates are not shown in figure 2.3 to ensure a better overview. There also exist other inverter circuits, but the full-bridge inverter is the most common. So, this paper only consider the full-bridge inverter.

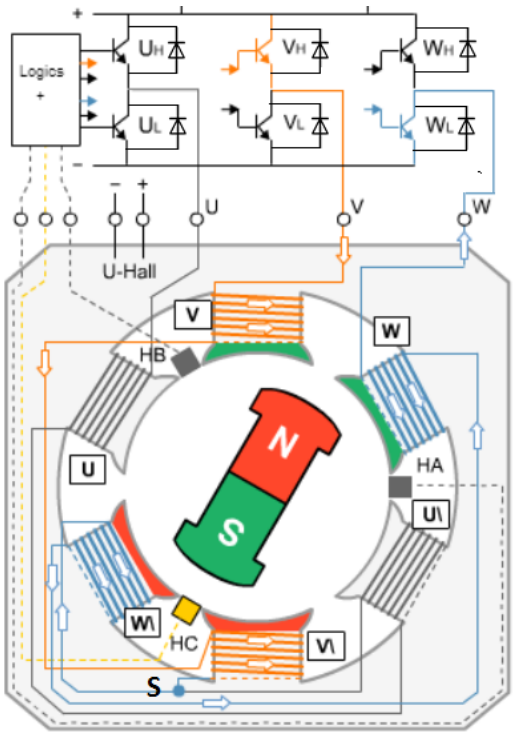

Figure 2.3: Drive Scheme of a BLDC motor including motor, inverter and hall sensors. [11]

2.2.1 Stator and Rotor

In a brushed DC motor the armature windings are located at the rotor and the magnet at the stator. Thus, an abrasive ring and brushes are needed to commutate the DC current in the armature windings. To remove these brushes the armature windings are installed at the stator in BLDC motors which can be compared to the stator structure of alternating current (AC) motors. But the armature windings are distributed in a way to produce trapezoidal back EMF waveforms. [8, pp. 25-28]

Figure 2.4 shows the back EMFs and the corresponding phase currents. The phase shift between each phase current and back EMF is 120° and the period is 360°.

The back EMF is induced in the stator windings due to the rotation according to Lenz's law. This back EMF opposes the supply voltage in each phase [12]. The rotation causes a change of magnetic flux. "Lenz's law states that whenever a change in a magnetic field occurs, an electric field is generated to oppose the change." [13, p. 75]

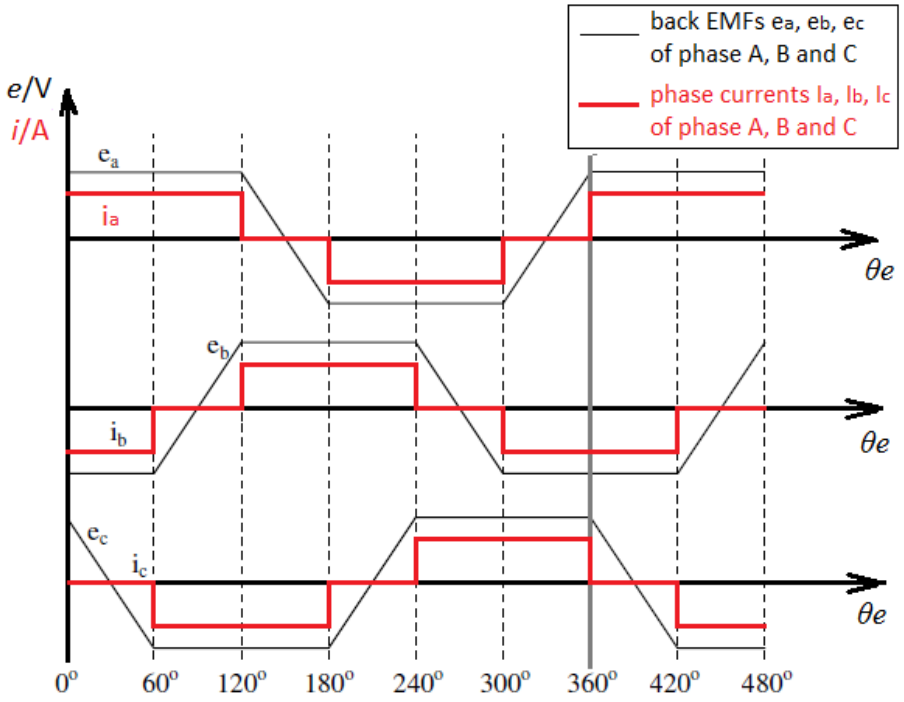

Figure 2.4: Current and back EMF waveforms of a BLDC motor. (modified from [10])

The equivalent electronic circuit diagram of the stator of a three-phase BLDC motor is shown in figure 2.5. Each winding consists of a resistance R, an inductance L and the corresponding back EMF e. [8] The so-called mutual inductance M between the phases is neglected in this paper. Furthermore, it is assumed that the value of each resistance and inductance is equal.

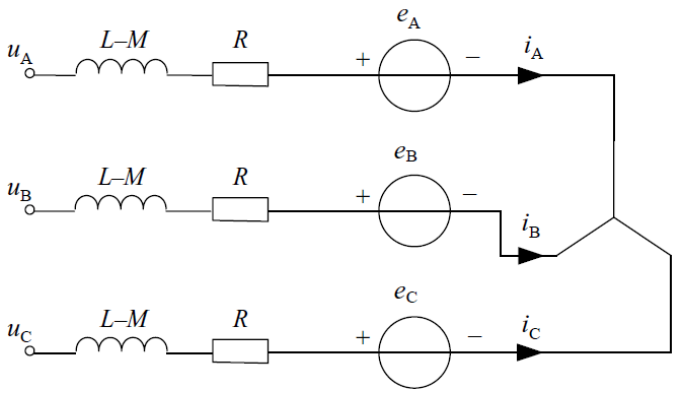

Figure 2.5: Equivalent electric circuit diagram of a three-phase BLDC motor. [8, p. 38]

The rotor is a iron core where permanent magnets are mounted and usually consists of 2 to 8 pole pairs. But the rotors of micro BLDC motors are only made out of 1 to 2 pole pairs. Rare-earth magnetic materials are used for the rotor which guarantee better magnetic properties like better coercivity and remanence. [8, p.27] Different structures of the rotor are possible. Since these structures would not change the results, they are not described in this paper, but can be looked up in [12].

2.2.2 Position Sensors and Sensorless Techniques

As already mentioned, the inverter needs a position information to produce the right switching sequence. The most popular position sensors are Hall sensors due to compact volume and low cost, but also optical sensors can be used [8]. Three Hall sensors are mounted either in the stator, as figure 2.3 shows, or on the rotor, which can be seen in figure 2.6. First mentioned needs an accurate positioning of the sensors during assembly to guarantee precise signals. Latter needs a scaled down version of the rotor magnets on the rotor shaft, which are called Hall sensor magnets and have the same orientation than the rotor magnets. The Hall sensors are fixed on a printed circuit board, which is connected to the stator. The sensor signals can be measured with the terminals. The advantage of the rotor-fixed Hall sensors is that the printed circuit board can be adjusted, so that the Hall sensor magnets and rotor magnets have the same orientation. The disadvantage is the more required space. [12]

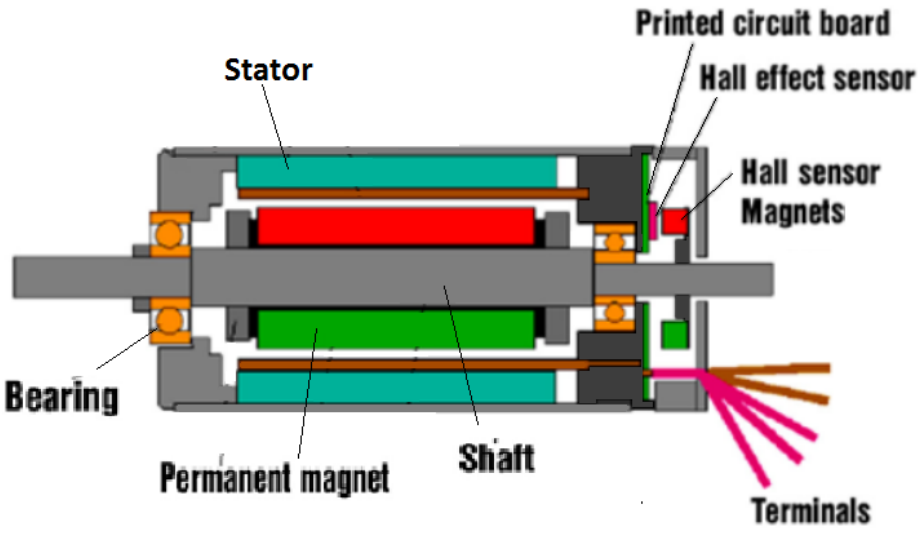

Figure 2.6: Tranverse section of a BLDC motor and Hall sensor magnets mounted on rotor shaft.(modified from [14]

)

The Hall sensors are based on the Hall effect, which is illustrated in figure 2.7. This Hall effect implies that the current *i* through a conducting plate (through A and B in figure 2.7), called Hall element, deflects to one side (to X in figure 2.7), if the plate is crossed by a perpendicular magnetic field. Thus, the so-called Hall voltage can be measured between the sides X and Y, which is perpendicular to both current and magnetic field. [15]

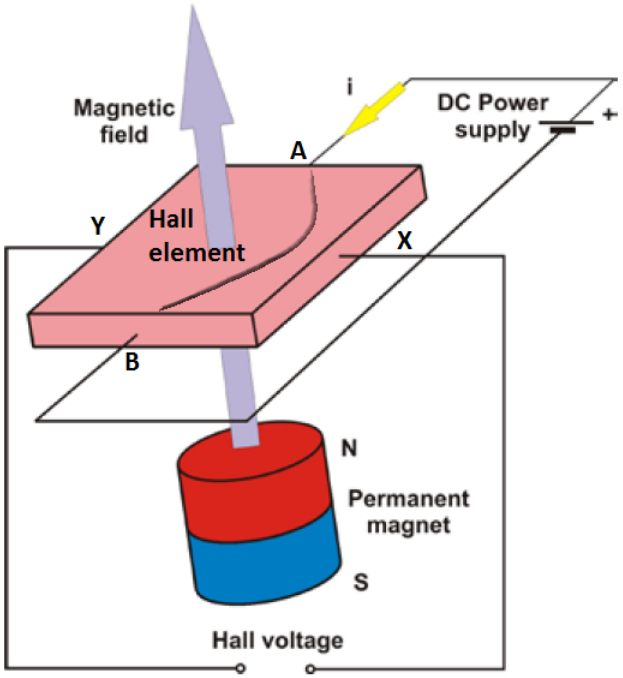

Figure 2.7: Illustration of the Hall effect. (modified from [14])

The Hall signals according to the rotor position are shown in table 2.1. A logic block generate the commutation sequence out of these signals.

rotor position	H1	H2	H3
0° - 60°	1	0	0
60° - 120°	1	1	0
120° - 180°	0	1	0
180° - 240°	0	1	1
240° - 300°	1	0	1
300° - 360°	0	0	1

Table 2.1: Hall-sensor signals according to rotor position. [1]

To eliminate the required space or the difficult assembly of the sensors sensorless techniques are developed. As figure 2.4 shows each back EMF crosses the time axis and thus be zero at 30° before the commutation of the current happens. Hence, this zero-crossing of the back EMF of the switched off phase can be detected and used to generate the commutation sequence. Several methods based on the zero-crossing detection of the back EMF like the terminal voltage sensing, the back EMF integration method, the third-harmonic back EMF method, the freewheeling diode method and the line back EMF method exist. But also other techniques than these back EMF based methods exist. The flux can be also regarded to obtain the rotor position. This is called the flux-linkage-based method. These two methods face problems during starting process because a certain rotational speed is needed to produce either the back EMF or flux. The inductance-based method eliminate this problem by comparing the current amplitudes. [8, pp. 168-206]

Furthermore, there also exist intelligence-based methods as artificial neural networks or fuzzy strategy. A more detailed description of these methods can be looked up in [8, pp. 168-206].

To simplify the BLDC motor model the position is obtained out of integrating the rotational speed of the rotor in this thesis.

2.2.3 Three-phase Full-bridge Inverter

There a two different drive modes, namely the two-phase conduction mode and the three phase conduction mode. Due to simplicity only the first mentioned is realized. Thus, two phases are always switched at any given moment, one of the upper bridge switch and one of the lower bridge switch but from different phase. Each switch is conducting for 120°. In figure 2.3 the switches V_H *and* W_L are activated. [8, pp. 30-31]

The inverter is a switch circuit which consists of power switches for example insulated bipolar gate transistor (IBGT) and diodes [7, pp. 136-142]. There are different types of inverter circuits [8, pp. 28-33], but this paper only refers to a three-phase full bridge inverter. The whole motor drive including BLDC motor, full bridge inverter and voltage supply is illustrated in figure 2.8. The commutation sequence of the three phases are generated out of the electrical angle according to table 2.2. The electrical angle is calculated by the rotor angle multiplied by the amount of pole pairs

$$\theta_e = \theta_m \cdot \frac{p}{2}, \tag{2.1}$$

where p is the number of poles.

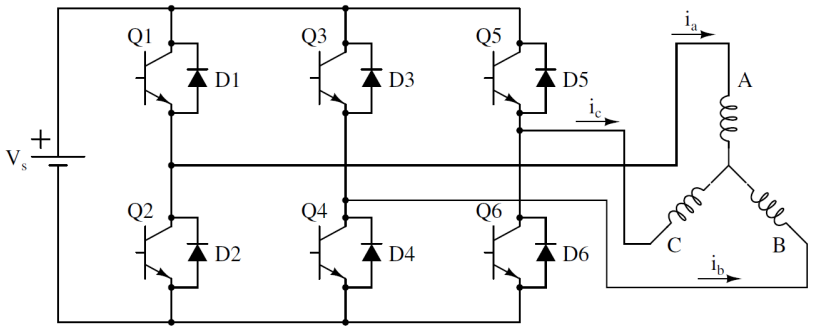

Figure 2.8: Motor drive scheme including a three-phase full bridge inverter. [1]

electrical angle	H1	H2	H3	closed Switches	Ia	Ib	Ic
0° - 60°	1	0	0	Q1 Q4	+	-	off
60° - 120°	1	1	0	Q1 Q6	+	off	-
120° - 180°	0	1	0	Q3 Q6	off	+	-
180° - 240°	0	1	1	Q3 Q2	-	+	off
240° - 300°	1	0	1	Q5 Q2	-	off	+
300° - 360°	1	0	1	Q5 Q4	off	-	+

Table 2.2: switching sequence according to rotor position and Hall-sensor signals. [1]

Table 2.2 shows that at any given moment the current flows into the motor in one phase and outside in another one. The third phase is switched off. If the switched off phase is switched on and a switched on phase is switched off, the current of the switched off phase passes the freewheeling diode. This freewheeling of a phase is shown in figure 2.9. Regarding table 2.2 the switches Q1 and Q4 are closed at a electrical angle of 0°-60°. Thus, a positive current flows in phase A and a negative current in phase B. At the next switching point Q6 is switched on and Q4 off. Thus, freewheeling of the negative conducting phase B through the diode D3 occurs. [16]

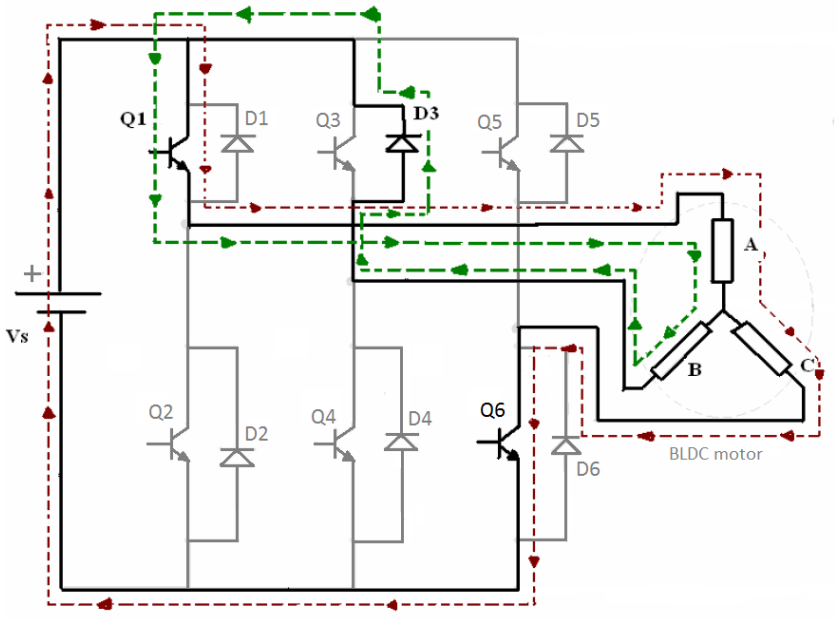

Figure 2.9: Freewheeling of negative conducting phase B. (modified from [16])

2.3 Advantages and Disadvantages

BLDC motors provide some advantages in contrast to other motors. In comparison to brushed DC motors BLDC motors have a longer lifetime due to electronic commutation. The mechanical commutation of brushed DC motors causes wear of the brushes. Furthermore, brush sparking can happen and the speed range is limited. Thus, less maintenance of BLDC motors is required. Additionally, the BLDC motor is more efficient and has a lower rotor inertia which enhances the dynamic response. The brushed DC motor has the windings on the rotor and the BLDC motor on the stator. Thus, the heat dissipation of BLDC motors is improved. The disadvantages are the higher costs and the more complex and expensive control of BLDC motors. The inverter always needs a controller for generating the switching sequence, but the same controller can be employed for speed control. [12]

Compared to AC induction motors the BLDC motor provide flat and linear speed/torque characteristics. The ratio of output power to size of the BLDC motor is higher. The AC induction motor has a poorer dynamic response than the BLDC motor and needs a starter circuit like a Star-Delta starter. Furthermore, no slip effect occurs in BLDC motors, which means that the rotor has the same frequency than the rotating magnetic field in the stator. The AC induction motor has an advantage for fixed speed applications, because no controller is required. [12]

Most similar to the BLDC motor is the PMSM. One advantage of the BLDC motor against the PMSM is the about 15% higher power density due to higher root-mean-square (rms) values of the currents. Furthermore, only two inverter switches are turned on for controlling the BLDC motor at every moment instead of all three for the PMSM. Thus, the drive system for BLDC motors causes less switching and conduction losses than the one for PMSM. Thermal reliability of the switching circuit is improved due to cooling the switches during switched-off mode. To produce the sinusoidal currents for PMSMs the position must be measured more accurate and the implementation is more complex. The only disadvantage of BLDC motors is the higher torque ripple compared to the PMSM.

2.4 Mathematical Modeling of the BLDC motor

The behavior of the BLDC motor can be described with differential equations, transfer functions or state-space equations. For simulation in MATLAB®/SIMULINK® the transfer function and state-space representation are preferred.

2.4.1 Differential Equations of the BLDC motor

Modeling of the BLDC motor is split up into an electrical and mechanical part. This paper shows the basic equations. A more detailed derivation of the equations can be looked up in [8, pp. 33-39]. The equivalent electric circuit of the stator of the BLDC motor can be seen in figure 2.5. Thus, the input voltages for a balanced system R_a=R_b=R_c=R and L_a=L_b=L_c=L and neglected mutual inductance are

$$v_a = R \cdot i_a + L \cdot \frac{\mathrm{d}i_a}{\mathrm{d}t} + e_a, \tag{2.2}$$

$$v_b = R \cdot i_b + L \cdot \frac{\mathrm{d}i_b}{\mathrm{d}t} + e_b, \tag{2.3}$$

$$v_c = R \cdot i_c + L \cdot \frac{\mathrm{d}i_c}{\mathrm{d}t} + e_c \tag{2.4}$$

where

v_a, v_b, v_c are the input phase voltages of phase A, B and C in V,
i_a, i_b, i_c are the phase currents of phase A, B and C in A,
e_a, e_b, e_c are the back EMF of phase A, B and C in V,
R is the phase resistance in Ω and
L is the phase inductance in H. [1]

In most applications the star-connected BLDC motor without a neutral phase is used. Thus, the phase voltages are difficult to determine. Therefore, the mathematical model considering the line voltages is more convenient. These line voltages are equal to the supply voltage for neglected switching losses in each appropriate time period. The equations for the line voltages are

$$v_{ab} = R \cdot (i_a - i_b) + L \cdot (\frac{\mathrm{d}i_a}{\mathrm{d}t} - \frac{\mathrm{d}i_b}{\mathrm{d}t}) + (e_a - e_b), \tag{2.5}$$

$$v_{bc} = R \cdot (i_b - i_c) + L \cdot (\frac{\mathrm{d}i_b}{\mathrm{d}t} - \frac{\mathrm{d}i_c}{\mathrm{d}t}) + (e_b - e_c), \tag{2.6}$$

$$v_{ca} = R \cdot (i_c - i_a) + L \cdot (\frac{\mathrm{d}i_c}{\mathrm{d}t} - \frac{\mathrm{d}i_a}{\mathrm{d}t}) + (e_c - e_a). \ [8, p.38] \tag{2.7}$$

The back EMF is described in section 2.2.1 and the waveform can be seen in figure 2.4. The change of magnetic field is proportional to the rotational speed of the rotor. Thus, the equations of the back EMFs are

$$e_a = \frac{k_e}{2} \cdot \omega \cdot f(\theta), \tag{2.8}$$

$$e_b = \frac{k_e}{2} \cdot \omega \cdot f(\theta - \frac{2\pi}{3}), \tag{2.9}$$

$$e_c = \frac{k_e}{2} \cdot \omega \cdot f(\theta + \frac{2\pi}{3}) \tag{2.10}$$

where

k_e is the back EMF constant in Vs/rad,
ω is the rotational speed of the rotor in rad/s and
f(θ) is a function, which describes the trapezoidal waveform of the back EMFs

and is described by

$$f(\theta) = \begin{cases} 1, & 0 < \theta < \frac{2\pi}{3} \\ 1 - \frac{6}{\pi} \cdot (\theta - \frac{2\pi}{3}), & \frac{2\pi}{3} < \theta < \pi \\ -1, & \pi < \theta < \frac{5\pi}{3} \\ -1 + \frac{6}{\pi} \cdot (\theta - \frac{5\pi}{3}), & \frac{5\pi}{3} < \theta < 2\pi \end{cases}, \tag{2.11}$$

where the function for phase B is 120° and for phase C 240° phase shifted. [1]

The input voltages do not completely produce the electrical power P_e which generate the electrical torque T_e. There are losses in the windings and thus, the electrical power is related to the back EMFs and equals

$$P_e = e_a \cdot i_a + e_b \cdot i_b + e_c \cdot i_c. \ [1] \tag{2.12}$$

The electrical torque T_e depends on the electrical power and the rotational speed. If the electrical power is substituted with equation (2.12) and the back EMFs are substituted with equation (2.11)

the electrical torque equals

$$T_e = \frac{P_e}{\omega} = \frac{1}{\omega} \cdot (e_a \cdot i_a + e_b \cdot i_b + e_c \cdot i_c) = \tag{2.13}$$

$$\frac{k_T}{2} \cdot [i_a \cdot f(\theta) + i_b \cdot f(\theta - \frac{2\pi}{3}) + i_c \cdot f(\theta + \frac{2\pi}{3})] \tag{2.14}$$

where k_T is the torque coefficient in Nm/A and k_T=k_e. [1] This is the maximum torque which is provided from the voltage source. This torque faces friction and a load torque can be applied. The electromechanical behavior of the BLDC motor is described with

$$T_e - T_L = J \cdot \dot{\omega} + B_f \cdot \omega \tag{2.15}$$

where

T_e is the electrical torque,

T_L is the load torque,

J is the rotor's moment of inertia,

$\dot{\omega}$ is the angular acceleration and

B_f is the viscous friction constant. [8, pp. 33-39]

2.4.2 Transfer Functions of the BLDC motor

For better control analysis the mathematical model based on transfer functions is considered. As in section 2.2.3 mentioned the two-phase conduction mode is analyzed. In this mode always two phases are turned on at every moment and thus,

$$i_a = -i_b = i, \tag{2.16}$$

$$\frac{\mathrm{d}i_a}{\mathrm{d}t} = -\frac{\mathrm{d}i_b}{\mathrm{d}t} = \frac{\mathrm{d}i}{\mathrm{d}t} \tag{2.17}$$

is applied for the period in which phase A and B are switched on. This equation is valid for all switching cycles. [8, pp. 40-45]

Therefore, the inverter can be neglected and equations (2.5)-(2.7) can be rearranged with equations (2.16) and (2.17) to

$$v_{ab} = V_{dd} = 2R \cdot i + 2L \cdot \frac{\mathrm{d}i}{\mathrm{d}t} + 2 \cdot e_a = r_a \cdot i + L_a \cdot \frac{\mathrm{d}i}{\mathrm{d}t} + k_e \cdot \omega \tag{2.18}$$

where

V_{dd} is the supply voltage,

r_a is the line to line resistance,

L_a is the line to line inductance. [8, pp. 40-45]

This equation is the same as for a brushed DC motor. The equivalent electrical circuit of equation (2.18) can be seen in figure 2.10. [8, pp. 40-45]

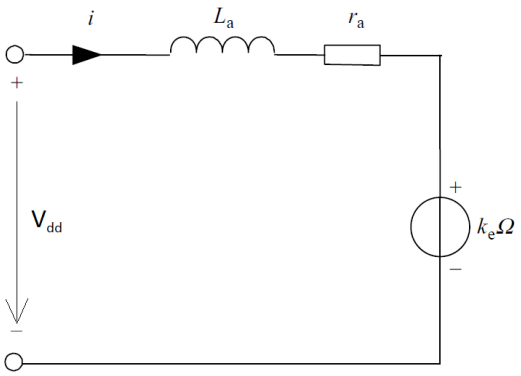

Figure 2.10: Equivalent electrical circuit of a BLDC motor with neglecting switching circuit in two-phase conduction mode. [8, p. 41]

Thus, the Laplace transformation is

$$V_{ab} - k_e \cdot \Omega \quad = \quad = I \cdot (r_a + L_a s) \tag{2.19}$$

and the transfer function

$$G_{s1}(s) \quad = \quad \frac{I}{V_{ab} - k_e \cdot \Omega} = \frac{1}{L_a s + r_a} \tag{2.20}$$

is obtained. The transfer function of equation (2.15) is

$$G_{s2}(s) \quad = \quad \frac{\Omega}{T_e - T_L} = \frac{1}{Js + B_f}. \; [8, pp. 40 - 45] \tag{2.21}$$

The block diagram of the BLDC motor with the obtained transfer functions can be seen in figure 2.11

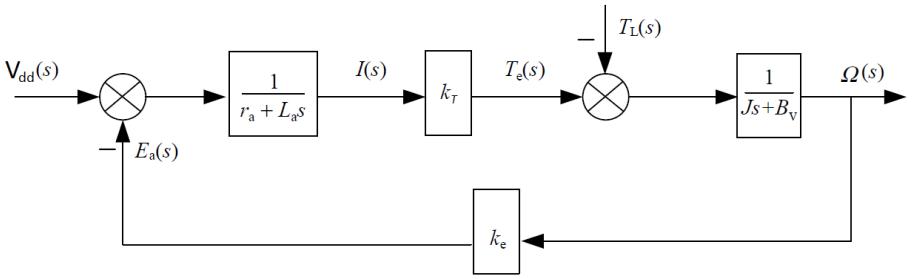

Figure 2.11: Block diagram of a BLDC motor with load torque as disturbance. (modified from [8, p. 45])

Thus, the whole transfer function without torque load is

$$G_{s_{motor}}(s) \quad = \quad \frac{\Omega}{V_{dd}} = \frac{k_T}{L_a J s^2 + (r_a J + L_a B_f)s + (r_a B_f + k_e k_t)}. \; [8, pp. 40 - 45] \tag{2.22}$$

2.4.3 State Space Representation of the BLDC motor

The importance of the state space representation has grown very much in recent years. New control techniques like optimal control theory, adaptive control and Kalman filters need the state space

representation. The control parameters are gained of the system matrices of these equations. The general state space representation is

$$\dot{x} = Ax + Bu, \tag{2.23}$$
$$y = Cx + Du \tag{2.24}$$

where

u is the input vector,
x is the state vector,
y is the output vector,
A is the system matrix,
B is the input matrix,
C is the output matrix and
D is the direct feed through matrix. [8, pp. 45-46]

To formulate the state space equation for the phase voltages of the BLDC motor equations (2.2)-(2.4) and equation (2.15) must be rearranged to obtain the state space equation

$$\begin{pmatrix} \dot{i_a} \\ \dot{i_b} \\ \dot{i_c} \\ \dot{\omega} \\ \dot{\theta_m} \end{pmatrix} = \begin{pmatrix} -\frac{R}{L} & 0 & 0 & 0 & 0 \\ 0 & -\frac{R}{L} & 0 & 0 & 0 \\ 0 & 0 & -\frac{R}{L} & 0 & 0 \\ 0 & 0 & 0 & -\frac{B_f}{J} & 0 \\ 0 & 0 & 0 & 1 & 0 \end{pmatrix} \begin{pmatrix} i_a \\ i_b \\ i_c \\ \omega \\ \theta_m \end{pmatrix} + \begin{pmatrix} \frac{1}{L} & 0 & 0 & 0 \\ 0 & \frac{1}{L} & 0 & 0 \\ 0 & 0 & \frac{1}{L} & 0 \\ 0 & 0 & 0 & \frac{1}{J} \\ 0 & 0 & 0 & 0 \end{pmatrix} \begin{pmatrix} v_a - e_a \\ v_b - e_b \\ v_c - e_c \\ T_e - T_L \end{pmatrix} \tag{2.25}$$

where θ_m is the rotor position of the BLDC motor which is needed for creating the switching sequence of the inverter. The state space equation for the line voltages of the BLDC motor is obtained with the rearrangement of equations (2.5)-(2.7), equation (2.15) and $i_a+i_b+i_c=0$ and is [8, pp. 45-46]

$$\begin{pmatrix} \dot{i_a} \\ \dot{i_b} \\ \dot{i_c} \\ \dot{\omega} \\ \dot{\theta_m} \end{pmatrix} = \begin{pmatrix} -\frac{R}{L} & 0 & 0 & 0 & 0 \\ 0 & -\frac{R}{L} & 0 & 0 & 0 \\ 0 & 0 & -\frac{R}{L} & 0 & 0 \\ 0 & 0 & 0 & -\frac{B_f}{J} & 0 \\ 0 & 0 & 0 & 1 & 0 \end{pmatrix} \begin{pmatrix} i_a \\ i_b \\ i_c \\ \omega \\ \theta_m \end{pmatrix} + \begin{pmatrix} \frac{2}{3L} & \frac{1}{3L} & 0 & 0 \\ 0 & \frac{2}{3L} & \frac{1}{3L} & 0 \\ \frac{1}{3L} & 0 & \frac{2}{3L} & 0 \\ 0 & 0 & 0 & \frac{1}{J} \\ 0 & 0 & 0 & 0 \end{pmatrix} \begin{pmatrix} v_{ab} - e_{ab} \\ v_{bc} - e_{bc} \\ v_{ca} - e_{ca} \\ T_e - T_L \end{pmatrix}. \tag{2.26}$$

The simplification of the BLDC motor with equations (2.16)-(2.17) and neglecting the inverter results in the state space equation

$$\begin{pmatrix} \dot{i} \\ \dot{\omega} \end{pmatrix} = \begin{pmatrix} -\frac{R}{L} & -\frac{k_e}{L} \\ \frac{k_T}{J} & -\frac{B_f}{J} \end{pmatrix} \begin{pmatrix} i \\ \omega \end{pmatrix} + \begin{pmatrix} \frac{1}{L} & 0 \\ 0 & -\frac{1}{J} \end{pmatrix} \begin{pmatrix} v \\ T_L \end{pmatrix}. \tag{2.27}$$

where the rotor position is not needed anymore. The controller only regulate the amplitude of the input voltage and not the load torque. To implement the optimal controller only for the input voltage the load torque is considered as disturbance. The general plant equations with disturbances are

$$\dot{x} = Ax + Bu + Gw, \tag{2.28}$$
$$y = Cx + Du + Hw + v \tag{2.29}$$

where

w is the disturbance vector,
v is the noise vector,
G is the disturbance matrix for the states,
H is the disturbance matrix for the output. [17]

The corresponding block diagram is shown in figure 2.12.

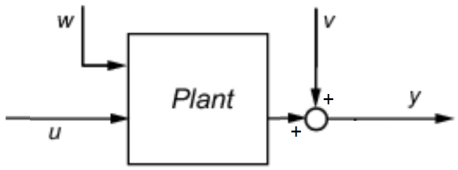

Figure 2.12: Block diagram of plant with disturbance w and noise v. [17]

Then equation (2.27) changes to

$$\begin{pmatrix} \dot{i} \\ \dot{\omega} \end{pmatrix} = \begin{pmatrix} -\frac{R}{L} & -\frac{k_e}{L} \\ \frac{k_T}{J} & -\frac{B_f}{J} \end{pmatrix} \begin{pmatrix} i \\ \omega \end{pmatrix} + \begin{pmatrix} \frac{1}{L} \\ 0 \end{pmatrix} v + \begin{pmatrix} 0 \\ -\frac{1}{J} \end{pmatrix} T_L \tag{2.30}$$

2.5 Losses of a BLDC motor

In general, the major losses in electric motors are the copper losses, iron losses, friction losses, windage losses and constant losses. The highest of these losses are the copper losses. This especially applies to small motors. These copper losses P_{L_c} are caused by the electrical current, which heats up the wires due to their electrical resistance. Thus, the copper losses result in

$$P_{L_c} = R \cdot I^2. \text{ [14]} \tag{2.31}$$

The current is proportional to the torque, like equation (2.14) shows. Therefore, the copper losses P_{L_c} can also be calculated with

$$P_{L_c} = k_c \cdot T_e^2 \tag{2.32}$$

where k_c is a constant copper loss factor. [14]

The iron losses comprise hysteresis losses and eddy current losses as well. The rotation of the rotor causes a change in the magnetic field. Thus, the iron of the rotor gets alternately magnetized and demagnetized, which results in hysteresis losses. These losses can be minimized with the use of high-quality iron. The change of magnetic field also generates eddy currents in the iron, which heat up the rotor. These are the eddy current losses and can be reduced by increasing the resistance of the iron core. This is done by using a laminated iron core instead of a solid one. The iron losses mainly depend on the frequency of the change of flux and thus, on the rotational speed of the rotor. That implies that the iron losses can be simplified as

$$P_{L_i} = k_i \cdot \omega \tag{2.33}$$

where k_i is a constant iron loss coefficient. [14]

The friction losses occur due to friction in the bearings and equals

$$P_{L_f} = B_f \cdot \omega^2 \tag{2.34}$$

with $P = T \cdot \omega$ and B_f as viscous friction constant. [14]

The windage losses are caused by the wind resistance of the rotor. A fan for cooling the rotor will cause higher windage losses. The windage loss torque is proportional to the square of the rotational speed. Therefore, the windage losses equals

$$P_{L_w} = k_w \cdot \omega^3 \tag{2.35}$$

with $P = T \cdot \omega$ and k_w as constant windage coefficient. [14]

The constant losses occur due to the power electronic circuit and are just a constant power loss C. Thus, the total power loss P_L is

$$P_L = P_{L_c} + P_{L_i} + P_{L_f} + P_{L_w} + C = k_c \cdot T_e^2 + k_i \cdot \omega + B_f \cdot \omega^2 + k_w \cdot \omega^3 + C \tag{2.36}$$

where the iron loss and windage coefficients are much smaller than the copper loss factor. [14]

3 Tractive Force for accelerating the Mobile Robot

The mobile robot is a small four-wheeled vehicle. The torque of the BLDC motor is related to the speed of the mobile robot. For simplicity it is assumed that only one BLDC motor is used to drive the four wheels. Depending on the desired speed and external forces acting on the mobile robot the motor torque needs to be regulated. Thus, this chapter describes the relationship between motor torque and the speed of the mobile robot.

All external forces which are acting on the mobile robot are shown in figure 3.1, where

F_{te} is the tractive effort force,
F_{la} is linear acceleration force,
F_{ad} is the aerodynamic drag
F_N is the normal force,
F_{rr} is the rolling resistance force,
F_{hc} is the hill climbing force,
ψ is the angle of the roadway to an imaginary horizontal plane,
mg is the weight of the mobile robot. [9]

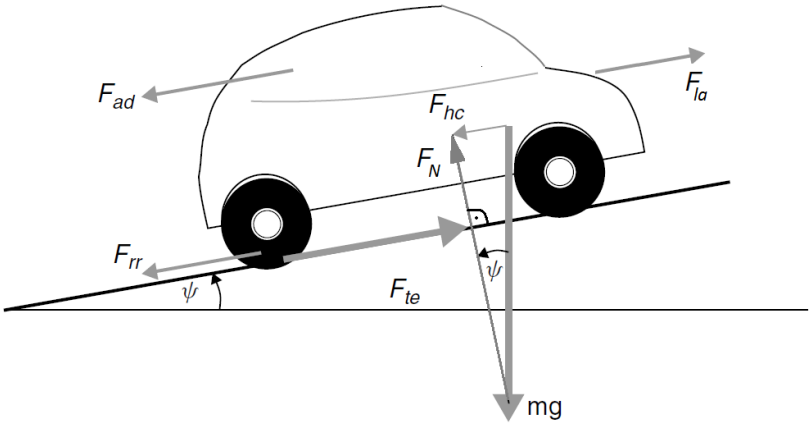

Figure 3.1: Forces acting on the mobile robot.(modified from [9])

The rolling resistance force F_{rr} is caused by friction between the wheels of the mobile robot and the road. It acts against the movement of the robot and is

$$F_{rr} = \mu_r \cdot F_N = \mu_r \cdot m \cdot g \cdot sin(\psi) \tag{3.1}$$

where

μ_r is the rolling resistance coefficient,
m is the mass of the mobile robot,
g is gravitational acceleration. [9, pp. 184]

The rolling resistance coefficient μ_r depends on the materials which are in contact, the tire pressure and the contact area. [9]

The aerodynamic drag F_{ad} is the wind resistance of the moving robot. This force is proportional to the square of the speed of the mobile robot and equals

$$F_{ad} = \frac{1}{2} \cdot \rho \cdot A \cdot k_{drag} \cdot v^2 \tag{3.2}$$

where

ρ is the density of the air,
A is the front area of the mobile robot,
k_{drag} is the drag coefficient,
v is the velocity of the mobile robot. [9]

The drag coefficient k_{drag} is a constant value and depends on the shape design of the vehicle. A common value is between 0.1 to 0.3. The air density and front area does not change and therefore, equation (3.2) can be simplified to

$$F_{ad} = K_d \cdot v^2 \tag{3.3}$$

with $K_d = \frac{1}{2} \cdot \rho \cdot k_{drag}$.

The hill climbing force F_{hc} is the force due to an inclined roadway. It decelerate the mobile robot driving up an ascent and accelerate it moving down a descent. This force is caused by gravitation and equals

$$F_{hc} = m \cdot g \cdot cos(\psi). \; [9, p.185] \tag{3.4}$$

The linear acceleration force F_{la} is the force to obtain the required acceleration. This force is derived from Newton's second law and equals

$$F_{la} = m \cdot a. \; [9] \tag{3.5}$$

To be more accurate the angular acceleration needed to speed up the rotor of the BLDC motor has to be also considered. This rotational acceleration is not shown in figure 3.1. Therefore, the relation between motor torque and tangential force is illustrated in figure 3.2.

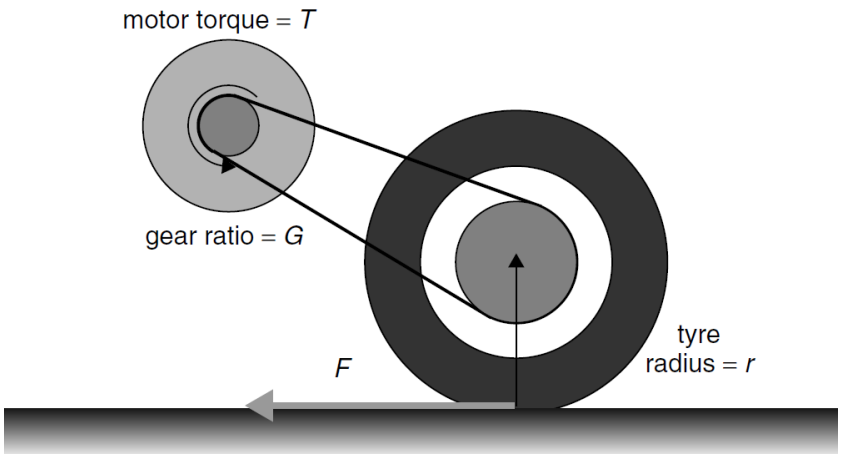

Figure 3.2: Transmission of motor torque to tangential force at the wheel. [9]

In general, the motor torque generates the tangential force

$$T = \frac{F \cdot r}{G_r} \tag{3.6}$$

where

T is the motor torque,
F is the tangential force,
r is the tire radius,
G_r is the gear ratio. [9]

The angular speed and acceleration of the motor can be described with

$$\omega = G_r \cdot \frac{v}{r} \tag{3.7}$$

$$\dot{\omega} = G_r \cdot \frac{a}{r} \tag{3.8}$$

where

ω is the angular speed of the motor,
$\dot{\omega}$ is the angular acceleration of the motor,
v is the speed of the mobile robot,
a is the acceleration of the mobile robot. [9]

With the use of equation (3.8) the torque $T_{\omega a}$, which accelerates the rotor of the motor, equals

$$T_{\omega a} = J \cdot \dot{\omega} = J \cdot G_r \cdot \frac{a}{r} \tag{3.9}$$

where J is the moment of inertia of the rotor. [9]

Substituting equation (3.11) into equation (3.9) results in

$$F_{\omega a} = J \cdot \dot{\omega} = J \cdot \frac{{G_r}^2}{r^2} \cdot a. \text{ [9]} \tag{3.10}$$

The whole tractive effort force F_{te} is the same as equation (3.11) and thus, can be calculated with

$$T_e = \frac{F_{te} \cdot r}{G_r}. \text{ [9]} \tag{3.11}$$

The tractive effort force is also equal to the sum of all forces from equations (3.1)-(3.10) and thus, results in

$$F_{te} = F_{rr} + F_{ad} + F_{hc} + F_{la} + F_{wa}. \text{ [9]} \tag{3.12}$$

Neglecting the rolling resistance and substitute equations (3.2)-(3.10) into equation (3.11) results in

$$T_m \cdot \frac{G_r}{r} = K_d \cdot v^2 + m \cdot g \cdot cos(\psi) + m \cdot a + J \cdot \frac{{G_r}^2}{r^2} \cdot a \tag{3.13}$$

with $T_m = T_e - T_L$. [9]

The term of the hill climbing force acts as a disturbance and can be neglected for now. Rearranging

equation (3.13) leads to

$$\dot{v} \cdot (m + J \cdot \frac{{G_r}^2}{r^2}) = \dot{v} \cdot K_v = T_m \cdot \frac{G_r}{r} - K_d \cdot v^2 \tag{3.14}$$

with $K_v = m + J \cdot \frac{{G_r}^2}{r^2}$. [9]

This is a nonlinear equation and needs to be linearized. The linearization around the operating point T_{e_0} and v_0 with the help of Taylor expansion

$$\Delta\dot{v} = \left.\frac{\delta f(T_m, v)}{\delta T_m}\right|_{T_{m_0}} \cdot \Delta T_m + \left.\frac{\delta f(T_m, v)}{\delta v}\right|_{v_0} \cdot \Delta v \tag{3.15}$$

leads to

$$\Delta\dot{v} = \frac{G_r}{r \cdot K_v} \cdot \Delta T_m - \frac{2 \cdot K_d}{K_v} \cdot v_0 \cdot \Delta v. \text{ [9]} \tag{3.16}$$

The Laplace transformation of equation (3.16) results to the transfer function

$$G_{s_{robot}} = \frac{\Delta v}{\Delta T_m} = \frac{\frac{G_r}{r}}{K_v \cdot s + 2 \cdot K_d \cdot v_0}. \tag{3.17}$$

This equation is integrated to obtain the position of the mobile robot. The position is the reference value of the closed loop. Including the hill climbing force results in

$$\Delta v = \Delta T_m \frac{G_r}{r} \cdot \frac{1}{K_v \cdot s + 2 \cdot K_d \cdot v_0} - m \cdot g \cdot cos(\psi) \cdot \frac{1}{K_v \cdot s + 2 \cdot K_d \cdot v_0}. \tag{3.18}$$

4 Controller Theory

The controller can face different challenges and objectives. Thus, the time and energy optimal motion is described first to get an overview what should be achieved with the energy optimal control. Furthermore, the basics of a proportional-integral-derivative (PID) controller are explained. The optimal control theory is used to implement the energy optimal control. Different strategies to regulate the input voltage of the BLDC motor are described and compared afterwards.

4.1 Time and Energy Optimal Motion

Various targets can be achieved with the control loop. The actual value can reach the desired value in optimal time or by consuming minimal energy. The time optimal control provides a comparison to determine if energy is saved with the energy optimal control.

The energy optimal motion is based on the minimization of the copper losses and thus, of

$$E_L = R \cdot \int_0^T i(t)^2 \mathrm{d}t \sim \int_0^T T_e(t)^2 \mathrm{d}t \sim \int_0^T \alpha(t)^2 \mathrm{d}t. \text{ [5]} \tag{4.1}$$

Figure 4.1 compares the time and energy optimal motions. The time optimal motion is characterized by a rapid increase to the maximum acceleration at starting time and remains at this value till half of the way is passed. Then, the acceleration jumps to the maximal negative value. It becomes zero when the desired position is reached. The velocity increases linearly for positive acceleration and decreases linearly when the acceleration becomes negative. The way has a parabolic waveform. In contrast, the energy optimal motion is determined by a linear decrease of the acceleration from the maximum value at starting time to the maximal negative acceleration at the final time. Thus, the velocity does not change linearly, but parabolic. The way of the energy optimal control has a cubical behavior. [5]

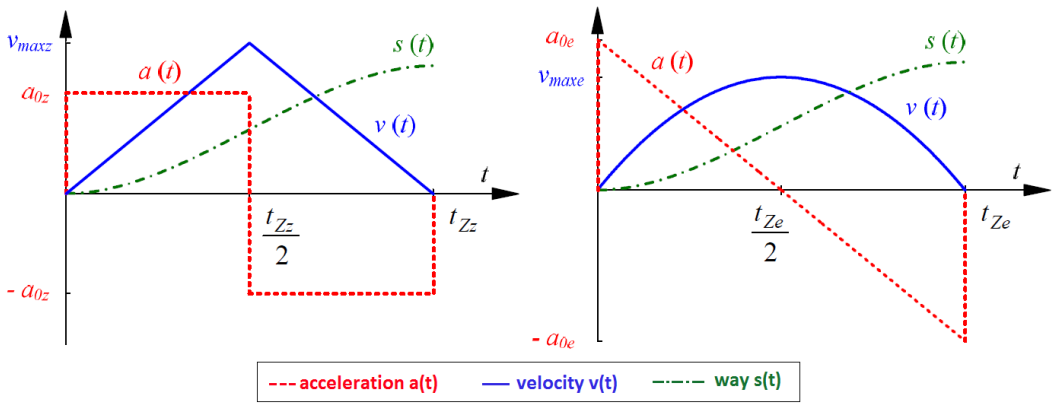

Figure 4.1: Acceleration, velocity and position over time for time optimal control (left) and energy optimal control (right). [5]

4.2 Time Optimal Controller

The time optimal controller is implemented with a PID controller. The PID controller is an important standard controller and is applied to a widespread field. The closed loop system with the PID controller can be seen in figure 4.2. The input of the PID controller is the control error e between desired value r and actual value y as input and the output is the actuating signal u. This controller combines the properties of a proportional (P), integral (I) and derivative (D) controller.

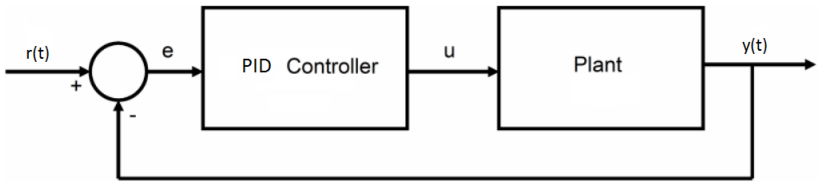

Figure 4.2: Closed loop system with PID controller. (modified from [18])

4.2.1 Proportional Controller

The P element amplifies its input with a proportional factor k_p. Thus, the the output is

$$x_a = k_p \cdot x_e \tag{4.2}$$

where x_e is the input and x_a is the output of the P element [19]. The step response of this element with $k_p = 3$ is shown in figure 4.3.

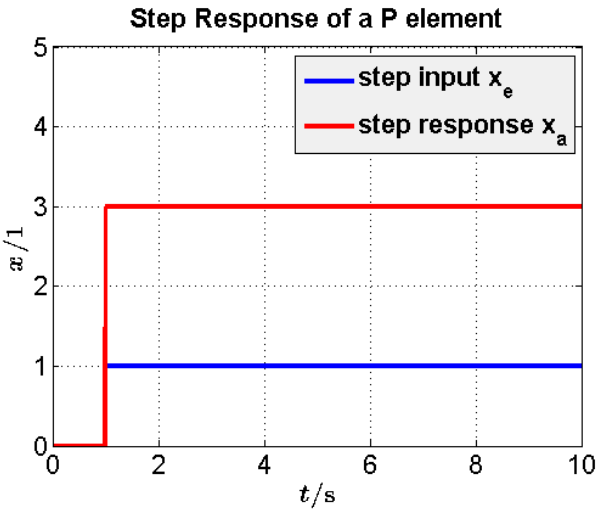

Figure 4.3: Step response of a proportional element.

The description of the closed loop is referred to figure 4.2. The P element as controller in a closed loop system amplifies the error with a proportional factor to calculate the actuating signal, which results in

$$u(t) = k_p \cdot e(t), \tag{4.3}$$

which equals

$$U = k_p \cdot E \tag{4.4}$$

in Laplace domain. [19]

The step response of the closed loop system with a P controller with $k_p = 3$ and an arbitrary controlled PT1 system is shown in figure 4.4.

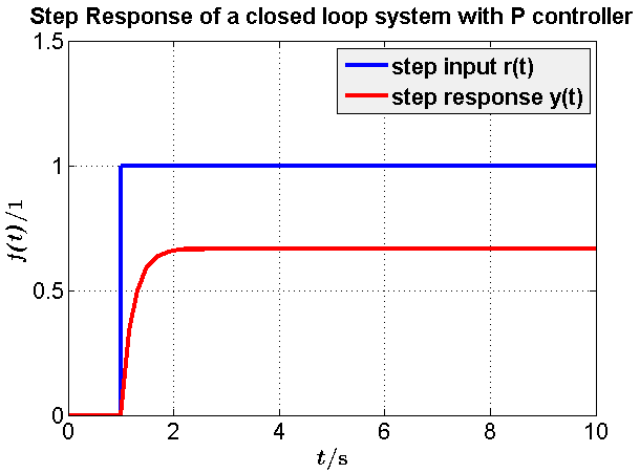

Figure 4.4: Step response of a closed loop system with a proportional controller.

The P controller provide a fast response. The disadvantage is that a steady-state error occurs. The error can be decreased by increasing the proportional factor k_p, but the error can not be completely eliminated.

4.2.2 Integral Controller

The output of the I element is the integration of the input. This leads to the equation

$$x_a = k_I \cdot \int_{t_0}^{T} x_e \cdot \mathrm{d}t \tag{4.5}$$

where k_I is the integral parameter. [19]

Figure 4.5 shows the step response of such an integral element with $k_I = 0.2$.

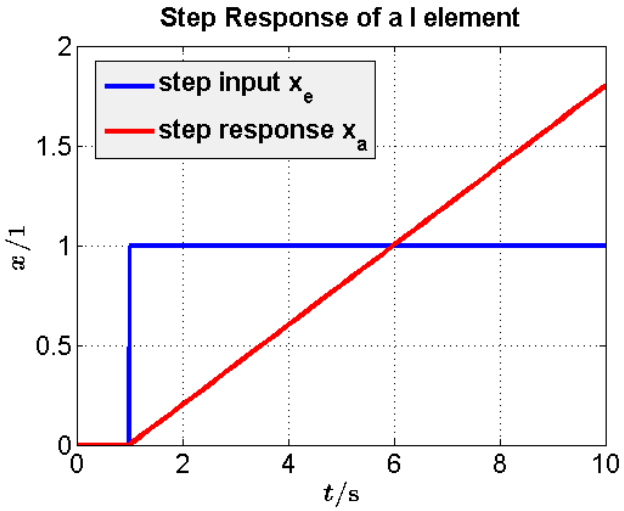

Figure 4.5: Step response of a integral element.

The integral element can be used as controller in a closed loop system as well. Then, the equation is given by

$$u(t) = k_I \cdot \int_{t_0}^{T} e(t), \tag{4.6}$$

which equals

$$U = \frac{k_I}{s} \cdot E \tag{4.7}$$

in Laplace domain. [19]

Figure 4.6 shows the step response of a closed loop system with an integral controller with $k_I = 3$ and an arbitrary controlled PT1 system.

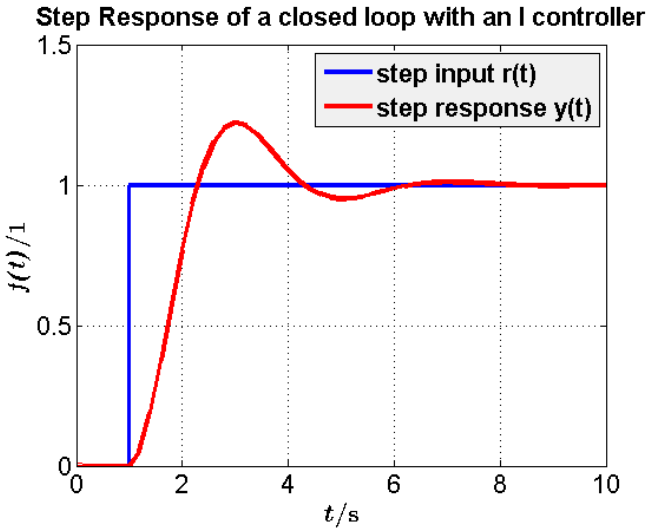

Figure 4.6: Step response of a closed loop system with an integral controller with $k_I = 3$.

If k_I is smaller, the reference value is reached without oscillation. This is shown in figure 4.7, where an integral controller with $k_I = 0.75$ is used.

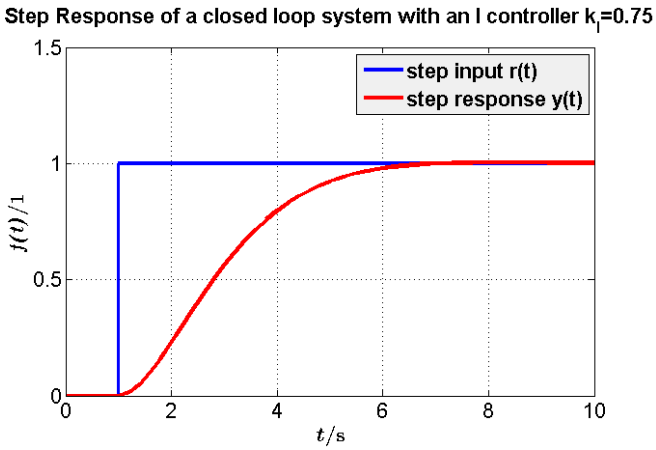

Figure 4.7: Step response of a closed loop system with an integral controller $k_I = 0.75$.

This controller changes the actuating value till the error disappears. Thus, it is very useful to eliminate the steady state error. [19]

4.2.3 Derivative Element

The output of the D element is the derivation of the input. This leads to the equation

$$x_a = k_D \cdot \dot{x_e} \tag{4.8}$$

or with the error as input and actuating value as output to

$$u(t) = k_D \cdot \dot{e(t)} \tag{4.9}$$

where k_D is the derivative parameter [19]. The Laplace transformation is

$$U = k_D \cdot s \cdot E \tag{4.10}$$

The step response of a D element with $k_D = 0.1$ is the so-called Dirac impulse and is shown in figure 4.8.

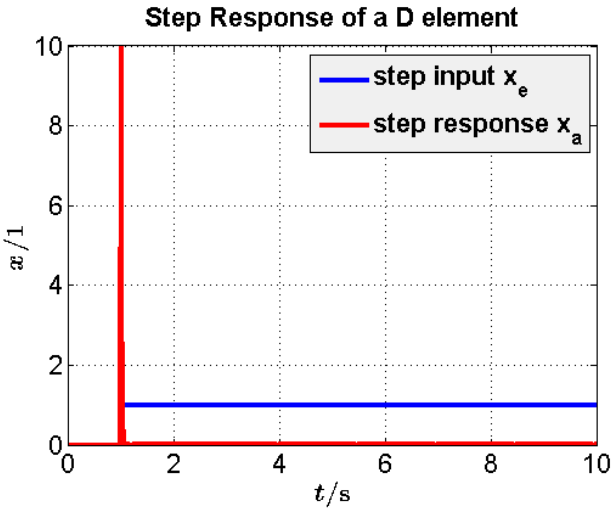

Figure 4.8: Step response of a derivative element.

The D element alone is not used as a controller because it amplifies noise. In practice it is combined with a P, I or both elements. It stabilizes the system and provides a quick reaction to abrupt changes of the control error.

The D element is not realizable in practice, because it is not possible to get an infinite impulse in zero time. Therefore, the derivative element with first order lag, called DT_1 element, is used. The behavior of this element is

$$U = \frac{k_D \cdot s}{T_V \cdot s + 1} \cdot E \tag{4.11}$$

where T_V is the delay time. [19]

The step response of this realizable derivative element with $k_D = 2$ and $T_V = 0.2$ is shown in figure 4.9.

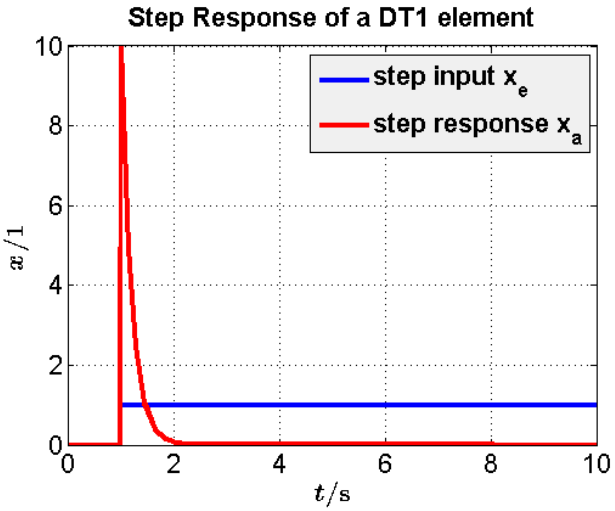

Figure 4.9: Step response of a realizable derivative element.

4.2.4 PID Controller

The behavior of the PID controller is the sum of equations (4.3)-(4.10) and equals to

$$u(t) = k_R \cdot e(t) + k_I \cdot \int_{t_0}^{T} e(t)\mathrm{d}t + k_D \cdot \dot{e(t)}. \text{ [19]} \tag{4.12}$$

Figure 4.10 shows the step response of a real PID element with an realizable derivative element with the parameters $k_P = 2, k_I = 0.5, k_D = 0.3$ and $T_V = 0.1$.

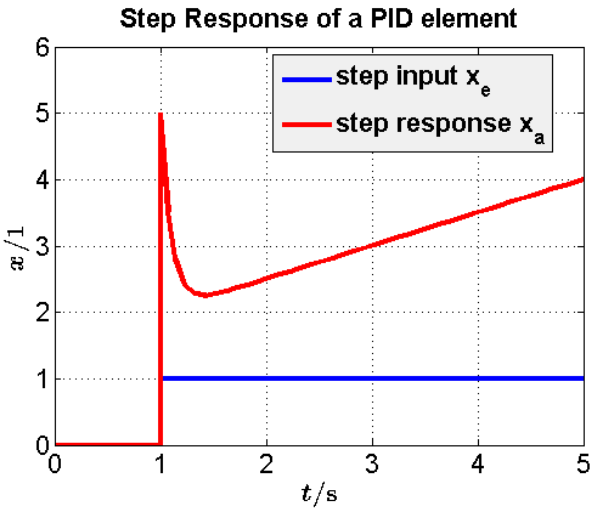

Figure 4.10: Step response of a real PID element.

A typical step response of the closed loop system with a PID controller is shown in figure 4.11 with the parameters $k_P = 5, k_I = 20, k_D = 0.1$ and $T_V = 0.01$.

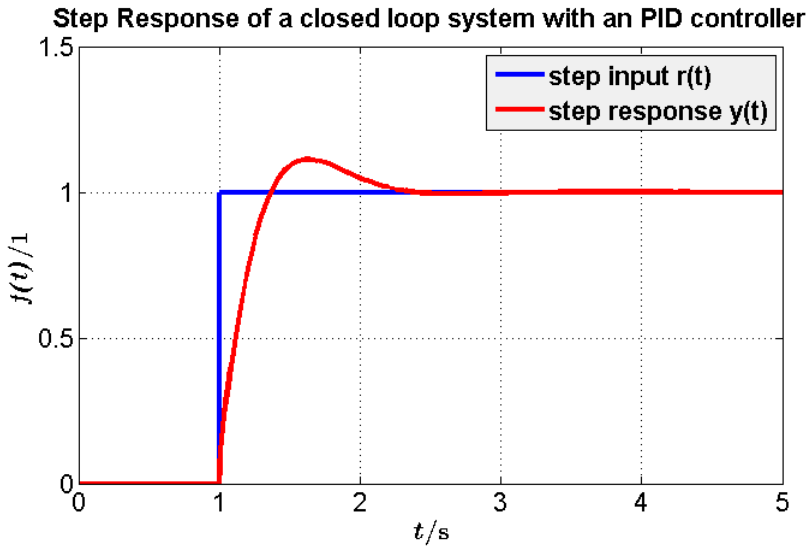

Figure 4.11: Step response of a closed loop system with an PID controller.

The PID controller combines the properties of the three elements. Thus, it has a fast response to changes of the desired value, no steady state error and a quick reaction on abrupt changes of the control error. [19]

There are different design rules to adjust the three parameters of a PID controller. These parameters can be adjusted manually, which needs some experience and can be very complex. Table 4.1 shows the effects of changing each parameter. The simplest procedure is the Ziegler Nichols method. At first, the parameters for the I and D element are zero. A small value for the proportional factor k_P is chosen and a step response of the desired signal is performed. Then k_P is increased till the step response starts oscillating. Afterwards, half of this factor is chosen and the parameters of the I and D element are determined out of the time period of the oscillation. Other procedures are the Chien-Hrones-Reswick, the symmetrical optimum or the modulus optimum method. [19]

Closed-Loop Response	Rise Time	Overshoot	Settling Time	Steady-State Error	Stability
Increasing K_P	Decrease	Increase	Small Increase	Decrease	Degrade
Increasing K_I	Small Decrease	Increase	Increase	Large Decrease	Degrade
Increasing K_D	Small Decrease	Decrease	Decrease	Minor Change	Improve

Table 4.1: Effects of adjusting P, I and D parameters. [20]

4.3 Energy Optimal Controller

The energy optimal controller is implemented with the help of the optimal control theory. This theory describes the optimal control of different criteria in general. It can be used for time, fuel or energy optimal control for example. This section only describes the energy optimal control theory in detail. Therefore, the so-called linear-quadratic-regulator (LQR) is used to increase the energy efficiency of the closed loop system.

4.3.1 Optimal Control Theory

The optimal control problem is formulated to obtain the optimal input u*(t) of the system, which influences the states x*(t) of the system such that the performance index is optimized and such that

$$\psi(x(T), T) \quad = \quad 0, \tag{4.13}$$

where

$\psi(x(T), T)$ is the fixed final function. In most practical cases the performance index is minimized instead of maximized. [21]

Generally, the system is supposed to have a nonlinear, time-varying behavior like

$$\dot{x} \quad = \quad f(x, u, t), t \geq t_0 \tag{4.14}$$

where x(t) is the state vector of size n and u(t) is the input vector of size m and the initial time t_0 is fixed. [21]

The general performance index or cost function equals

$$J(t_0) \quad = \quad \phi(x(T), T) + \int_{t_0}^{T} L(x(t), u(t), t)\mathrm{d}t \tag{4.15}$$

in a time interval $[t_0, T]$, where

$\phi(x(T), T)$ is the final weighting function depending on the final state and final time and
L(x(t),u(t),t) is the weighting function depending on the state, input and time. [21]

The aim is to minimize this performance index and thus, to keep $\phi(x(T), T)$ and L(x(t),u(t),t) small. The performance index can be chosen according to which control objective has to be achieved. For minimum time problems, where the final state is reached in minimal time, the performance index equals

$$J = T = \int_0^T 1 \cdot \mathrm{d}t, \tag{4.16}$$

where either ϕ=T and L=0 or Φ=0 and L=1 is possible. [21]

The concern of minimum fuel problems is to minimize the magnitude of the control vector because the fuel consumption has a proportional relationship to that. Thus, the performance index is

$$J = \int_{t_0}^T |u| \cdot \mathrm{d}t, \tag{4.17}$$

with $\phi = 0$ and $L = |u|$. [21]

Energy optimal problems usually are about minimizing the control effort. If the input u is the voltage from a voltage source, the energy loss is minimized by minimizing the performance index

$$J = \int_{t_0}^T u^2 \cdot \mathrm{d}t \tag{4.18}$$

with $\phi = 0$ and $L = u^2$. [22]

Another performance index for energy optimal problems is

$$J = \frac{1}{2} x(T)^T S x(T) + \frac{1}{2} \int_{t_0}^T (x^T Q x + u^T R u) \cdot \mathrm{d}t \tag{4.19}$$

with $\phi = \frac{1}{2} x(T)^T S x(T)$ and $L = \frac{1}{2}(x^T Q x + u^T R u)$. Q, R and S are weighting matrices where Q and S are symmetric and positive semi-definite and R is symmetric and positive definite. [21]

This is the so-called linear-quadratic-regulator (LQR). The aim is to find an input u, which minimizes the energy of the intermediate state, the final state and the control input itself. If the weighting matrix Q is chosen large, the focus is on keeping the intermediate state small. If a small control input is more important, the matrix R has to be large. A large matrix S implies that a small final state is more significant. Thus, the LQR can be adjusted depending on the requirements. [21]

The optimal controller is based on the so-called Hamiltonian function

$$H(x, u, t) = L(x, u, t) + \lambda^T \cdot f(x, u, t), \tag{4.20}$$

where

H(x,u,t) is Hamiltonian function,
L(x(t),u(t),t) is the weighting function of the general performance index,
λ is the so-called Lagrange multiplier or costate of the system and
f(x,u,t) is the function of the nonlinear, time-varying system. [21]

With the help of the calculus of variation the following conditions can be derived out of the increment of the derivation of the performance index $\mathrm{d}J^{'}$ and calculated with the derivation of the Hamiltonian function. The detailed derivation can be looked up in [21]. The first condition is the state equation, which equals

$$\dot{x} = \frac{\delta H(x,u,t)}{\delta \lambda} = f(x,u,t) \tag{4.21}$$

with $t \geq t_0$. [21]

The second equation is the costate equation and results in

$$-\dot{\lambda} = \frac{\delta H(x,u,t)}{\delta x} = \frac{\delta L(x,u,t)}{\delta x} + \frac{\delta f(x,u,t)^T}{\delta x} \cdot \lambda \tag{4.22}$$

with $t \leq T$. [21]

The stationary condition is the third equation, which is derived from the Hamiltonian function. This condition can be calculated with

$$0 = \frac{\delta H(x,u,t)}{\delta u} = \frac{\delta L(x,u,t)}{\delta u} + \frac{\delta f(x,u,t)^T}{\delta u} \cdot \lambda. \text{ [21]} \tag{4.23}$$

The boundary conditions are

$$(\phi_x + \psi_x^T \nu - \lambda)^T\big|_T \cdot \mathrm{d}x(T) + (\phi_t + \psi_t^T \nu + H)\big|_T \cdot \mathrm{d}T \quad = \quad 0. \text{ [21]} \tag{4.24}$$

and that $x(t_0)$ is given, where ν is an associated multiplier to the fixed final function $\psi(x(T),T)$ and where $\phi_x = \frac{\delta \phi}{\delta x}$, $\psi_x = \frac{\delta \psi}{\delta x}$, $\phi_t = \frac{\delta \phi}{\delta t}$ and $\psi_t = \frac{\delta \psi}{\delta t}$. [21]

4.3.2 The Linear-Quadratic-Regulator

The LQR is based on the linear system in state space representation shown in equation (2.24)

$$\dot{x} \quad = \quad Ax + Bu \tag{4.25}$$

and the performance index shown in equation (4.26)

$$J \quad = \quad \frac{1}{2} x(T)^T S x(T) + \frac{1}{2} \int_{t_0}^{T} (x^T Q x + u^T R u) \cdot \mathrm{d}t, \tag{4.26}$$

where these equations are reproduced here for convenience. [21]

The Hamiltonian function for the LQR equals

$$\begin{aligned} H(x,u,t) &= L(x,u,t) + \lambda^T \cdot f(x,u,t) = \\ &= \frac{1}{2}(x^T Q x + u^T R u) + \lambda^T (Ax + Bu). \text{ [21]} \end{aligned} \tag{4.27}$$

The Hamiltonian matrix H is a constant if the system and performance index are time-invariant.

Applying the state, costate and stationary condition results in

$$\dot{x} = \frac{\delta H(x,u,t)}{\delta \lambda} = Ax + Bu, \tag{4.28}$$

$$-\dot{\lambda} = \frac{\delta H(x,u,t)}{\delta x} = Qx + A^T\lambda, \tag{4.29}$$

$$0 = \frac{\delta H(x,u,t)}{\delta u} = Ru + B^T\lambda. \text{ [21]} \tag{4.30}$$

The optimal control u can be calculated in terms of the costate by solving equation (4.30) to

$$u(t) = -R^{-1}B^T\lambda(t), \tag{4.31}$$

which can be substituted into equation (4.28) resulting in

$$\dot{x} = Ax - BR^{-1}B^T\lambda. \text{ [21]} \tag{4.32}$$

A closed loop control can be achieved by allowing a free final state x(T). The final time T is fixed and given. Thus, $dx(T) \neq 0$ and dT=0. Substituting this into equation (4.24) results in

$$(\phi_x + \psi_x^T\nu - \lambda)^T\big|_T \cdot \mathrm{d}x(T) = (\phi_x - \lambda)|_T = 0. \text{ [21]} \tag{4.33}$$

Rearranging this equation leads to

$$\lambda(T) = \frac{\delta\phi}{\delta x}\bigg|_T = S(T) \cdot x(T) \tag{4.34}$$

with $\phi = \frac{1}{2}x(T)^T S x(T)$. [21]

It is assumed that this relationship holds on for the whole time interval [t_0,T]

$$\lambda(t) = S(t) \cdot x(t), \tag{4.35}$$

where the matrix function S(t) has to be found which proves this assumption. [21]

The derivation of this equation and substituting equation (4.32) results in

$$\dot{\lambda} = \dot{S}x + S\dot{x} = \dot{S}x + S(Ax - BR^{-1}B^T\lambda). \text{ [21]} \tag{4.36}$$

Then, $\dot{\lambda}$ is replaced by the costate equation (4.29) and equation (4.35) is used to substitute λ. This leads to

$$-Qx - A^TSx = \dot{S}x + S(Ax - BR^{-1}B^TSx), \tag{4.37}$$

which can be rearranged to obtain

$$-\dot{S}x = (A^TS + SA - SBR^{-1}B^TS + Q)x. \text{ [21]} \tag{4.38}$$

Canceling the state x results in the so-called matrix Riccati equation

$$-\dot{S} = A^TS + SA - SBR^{-1}B^TS + Q. \text{ [21]} \tag{4.39}$$

The assumption in equation (4.35) is proved, if S(t) is the solution of the Riccati equation with S(T) as the final condition. [21]

Therefore, equation (4.35) can be substituted into equation (4.31) and then, the optimal control can be calculated with

$$u(t) = -R^{-1}B^{T}Sx(t) = -K(t)x(t) \tag{4.40}$$

where $K = R^{-1}B^{T}S(t)$ is the Kalman gain. [21]

The optimal control problem is based on solving the Riccati equation (4.39) and calculating the Kalman gain. The Riccati equation has to be integrated backward. These two equations are solved offline, before it is applied to the system. The optimal control u*(t) is obtained out of the stored Kalman gain according to equation (4.40). [21]

If the system matrices A and B are time-invariant, $\dot{S}$=0 in the Riccati equation. Thus, the Kalman gain is a constant matrix and does not change over time. [21]

The block diagram of an LQR control system is shown in figure 4.12. The LQR does not follow any reference value and just keeps the states and the control input small. [21]

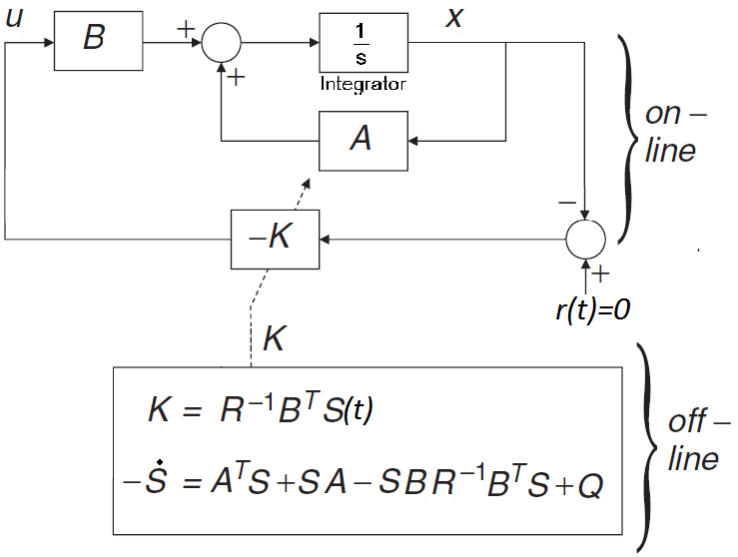

Figure 4.12: Block diagram of an LQR control system. (modified from [21])

Thus, an LQ integrator is used, so that the mobile robot follows the reference position. MATLAB®/SIMULINK® provides a command to calculate the solution of the Riccati equation and the Kalman gain for the LQ integrator for the given state space equation. The block diagram of a LQ integral control system is shown in figure 4.13. This control system can be compared to the control system in figure 4.2. The Kalman gain is multiplied with the states and the integrated error. The error equals the difference between the reference and output signal. [23]

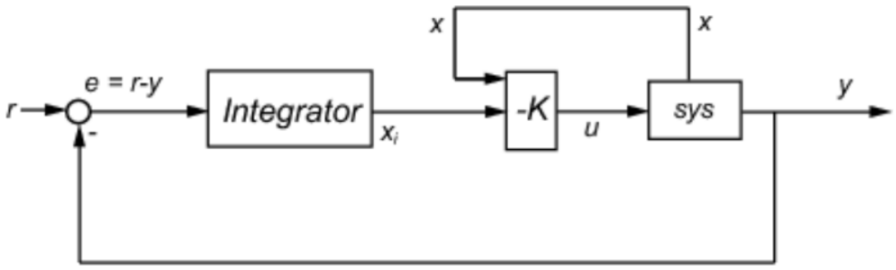

Figure 4.13: Block diagram of an LQ integrator control system. [23]

4.4 Control Strategies

There are different strategies to regulate the input voltage of a BLDC motor. The hysteresis band control is the simplest way. Other strategies are the pulse-width-modulation (PWM) control and the variable DC-link voltage control. The supply voltage is fixed for the hysteresis band and PWM control. [1]

4.4.1 Hysteresis Band Control

The hysteresis band control is a flip-flop control, where the inverter switches are switched off if the controlled signal exceeds a determined level above the reference value and turned on if the controlled signal falls below a specified level under the reference value. These levels are called the hysteresis band. The width of this hysteresis band can be chosen. For implementation in MATLAB®/SIMULINK® the relay block is used to generate the chopping signal. There are two different switching methods available. The hard chopping is based on switching off and on the conducting inverter switches according to table 2.2. By the soft chopping method only the upper switch of the conducting inverter switches according to table 2.2 is turned on and off. This results in less torque ripple and switching losses. But three PWM signals are needed for hard chopping and six PWM signals for soft chopping. Position control can not be implemented with the hysteresis band control because the direction of rotation has to be changed to hold the position within the band. This stresses the parts of the BLDC motor. [1]

Choosing the width of the hysteresis band has to be done carefully. If the hti97es occurs and a wider band results in large ripples. Thus, properties like switching frequencies, amplitude of the ripples and speed of the switching devices have to be taken into account when choosing the width of the hysteresis band. [24]

The switching frequencies varies with the applied load. Therefore, filtration of acoustic and electromagnetic noise is challenging if load variations occur. [25]

4.4.2 PWM Control

In the pulse width modulation control the output of the controller is compared to a carrier signal with a fixed, high frequency. In practice, the triangular carrier waveform like in figure 4.14(a) is the most common. The modulating controller output signal is compared to the carrier signal with a comparator. In figure 4.14(a) the modulating signal is a sine wave. If the carrier signal is less than

the modulating signal the output of the comparator is high. The output of the comparator is low if the carrier signal exceeds the modulating signal. These changing high-low signals are the resulting chopping signal of the PWM method, which is shown in figure 4.14(b). Signal 1 means the higher switch of the inverter is chopped and the lower switch is chopped for a signal -1. [26]

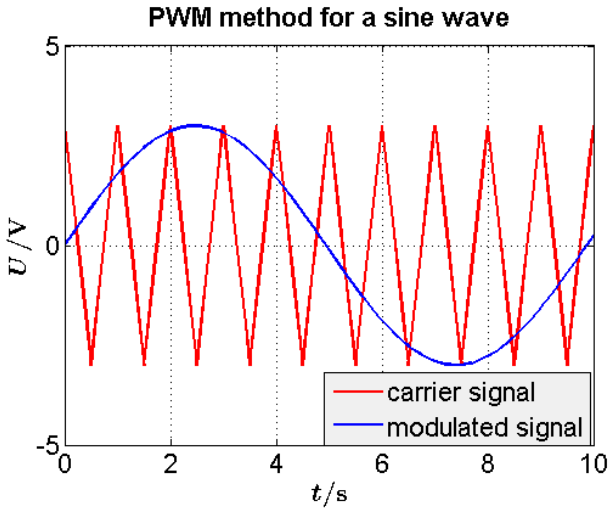

(a) Carrier and modulating signal of PWM method.

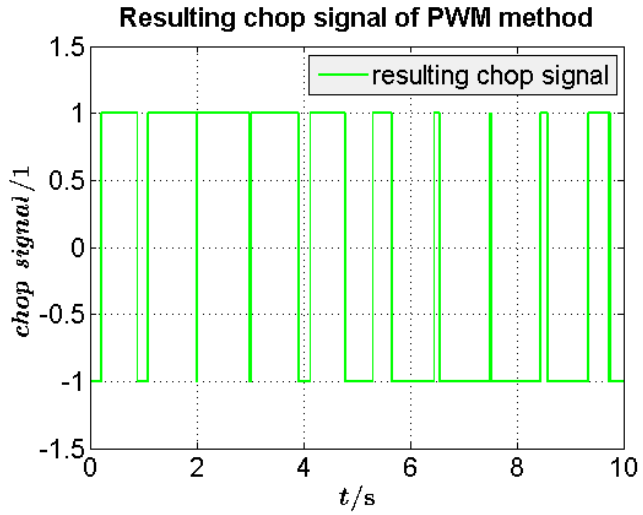

(b) Resulting chopping signal of PWM method.

Figure 4.14: Carrier, modulating and resulting chopping signal of the PWM method.

The PWM control also allows both hard and soft chopping, where soft chopping reduces torque ripple and switching losses again. The advantage of the PWM control towards hysteresis band control is the fixed switching frequency. Only the duty cycles change with the PWM method. Thus, the filtration of acoustic and electromagnetic noise is easier. [25]

4.4.3 Variable DC-link Voltage Control

The variable DC-link voltage control is implemented with a DC-DC converter between the voltage source and the inverter, which can be seen in figure 4.15. This DC-DC converter can be a buck or buck-boost converter for example. PWM is used to control the switches of the converter and thus,

the DC voltage is regulated. The output voltage of the converter is smoothed with a capacitor. Therefore, ripple is reduced compared to the PWM control of the inverter. The disadvantage is that an additional DC-DC converter is needed. [27]

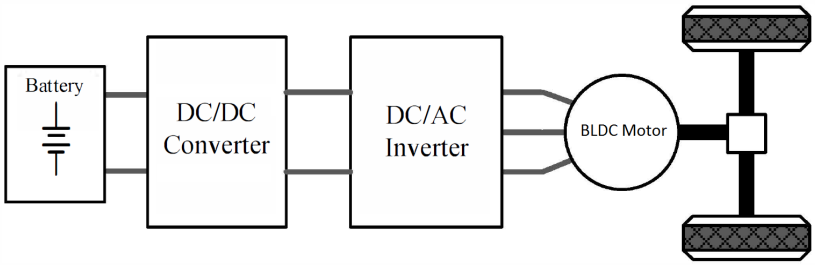

Figure 4.15: Block diagram of a Variable DC-link voltage control. (modified from [27])

The circuit and the principle of a buck converter can be seen in figure 4.16. The switch T1 is pulse-width-modulated, which results in a regulated DC voltage v_0. The output of the controller is compared to the carrier signal and generate the chopping signal for the switch T1. [28]

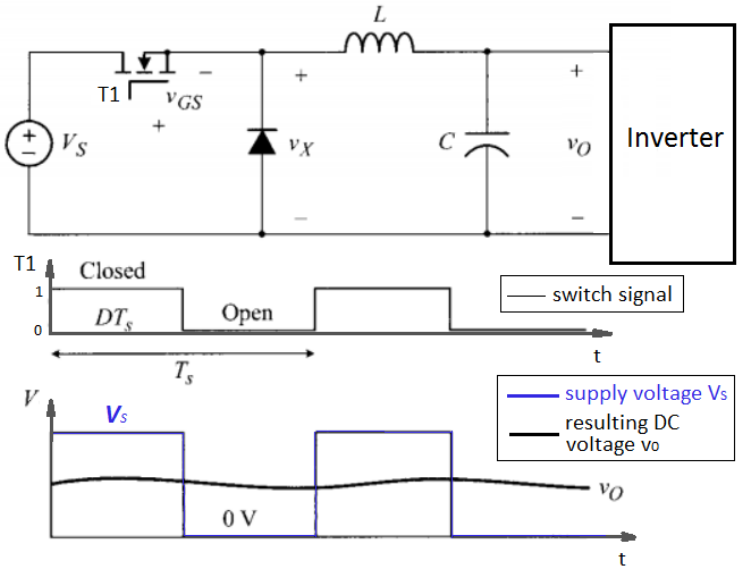

Figure 4.16: Circuit and principle of a buck converter. (modified from [28])

In the PWM control in previous section a considerable commutation delay can occur especially by high speeds. The reason is that the commutation of the inverter and the PWM are not executed independently. Therefore, the variable DC-link voltage control can be implemented to eliminate this commutation delay. [29]

In MATLAB®/SIMULINK® the output of the controller can be used as variable voltage. Thus, no PWM is needed for the simulation, but has to be implemented if the simulation is tested on the real motor. [1]

5 MATLAB®/SIMULINK® Implementation

MATLAB®/SIMULINK® is used to simulate the BLDC motor and the speed of the mobile robot. First, the simplified transfer function model of the BLDC motor is implemented to figure out the missing parameters of the data sheet. The model is verified by plotting the rotational speed, current, mechanical power and efficiency over the torque. These diagrams describe the behavior of the motor. Secondly, the whole BLDC motor drive model is simulated and validity is proved. Then, the behavior of the mobile robot is added to the motor model and time and energy optimal control is implemented.

5.1 Simplified BLDC Motor Model

This model is implemented like in figure 2.11. Therefore, the transfer function equations (2.20)-(2.21), $T_e = k_T \cdot i$ and $e_a = k_e \cdot \omega$ are needed. The simulation model is shown in figure 5.1. The rotational speed, torque, current, mechanical output power and the efficiency are measured for the verification of the model.

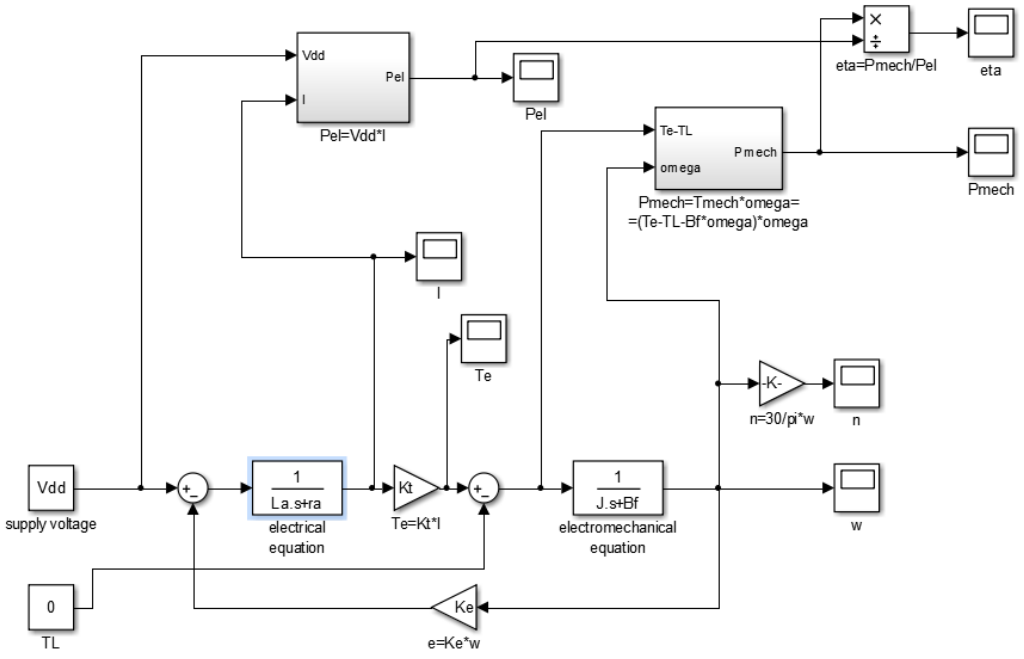

Figure 5.1: SIMULINK® model of the simplified BLDC motor.

5.2 Whole BLDC Motor Drive Model

This section describes the modeling of the BLDC motor, the inverter and the logic to control the inverter switches. The position, which is used for generating the switching sequence of table 2.2, is

obtained by integrating the angular velocity. The BLDC motor drive model is referred to [1].

The simulation model of the BLDC motor drive is shown in figure 5.2. The switch logic block generates the signal for each inverter switch according to table 5.1, which can be deduced from table 2.2. The posit)ion equals the angle θ of the rotor, but starts at zero after 360°. The switch logic block just compares the position with the rotor position values in table 5.1 and generate the switch signals out of that.

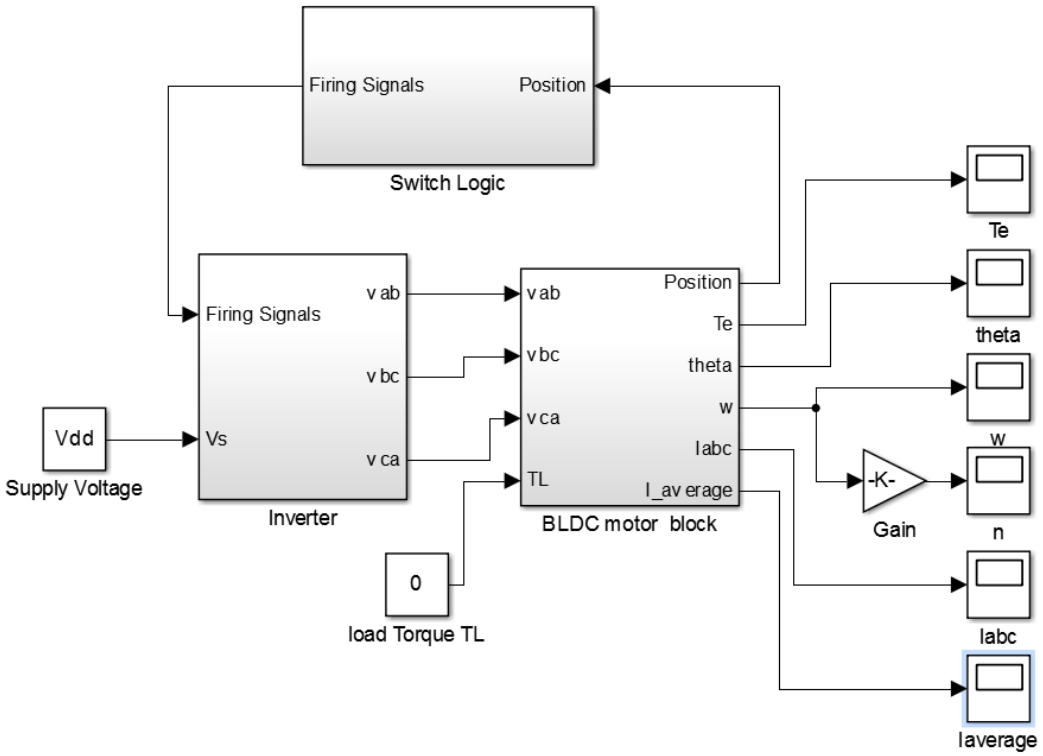

Figure 5.2: SIMULINK® model of the whole BLDC motor drive.

rotor position	Switch ON
0° - 120°	Q1
60° - 180°	Q6
120° - 240°	Q3
180° - 300°	Q2
240° - 360°	Q5
300°-360° and 0°-60°	Q4

Table 5.1: Inverter switch signals as output of the switch logic block. (modified from [1])

The BLDC motor block is based on the state space equation (2.26). This equation is implemented in the state-space equation block in figure 5.3. The back EMF of each phase is calculated with equations (2.8)-(2.10). Then, the back EMFs between two phases are calculated and subtracted to the input voltages. The trapezoidal functions of equation (2.11) and the corresponding phase shift are implemented with look-up tables, which is shown in figure 5.4. The rotor angle θ is transformed to the electrical angle with the factor $\frac{p}{2}$ and the position starts from zero after reaching 360°. The torque is calculated with equation (2.14). The average of the current is calculated for the current-torque diagram.

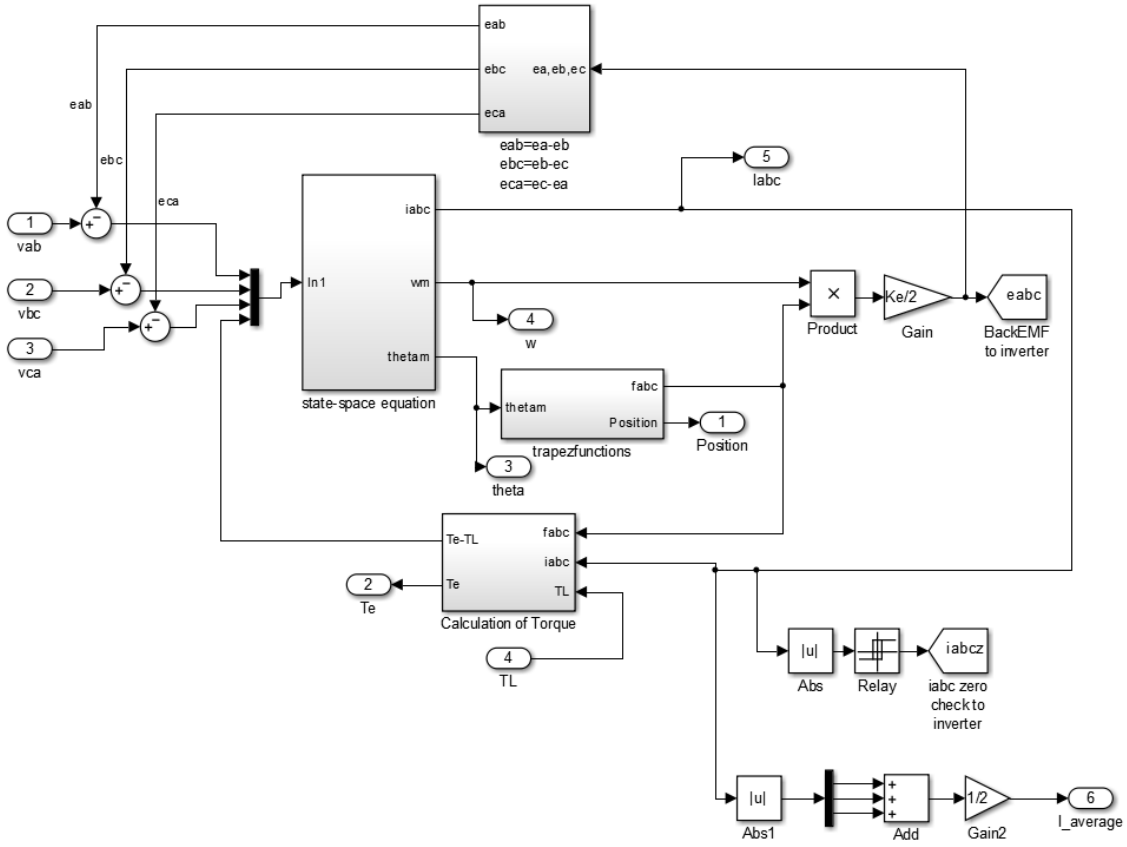

Figure 5.3: SIMULINK® block of the BLDC motor.

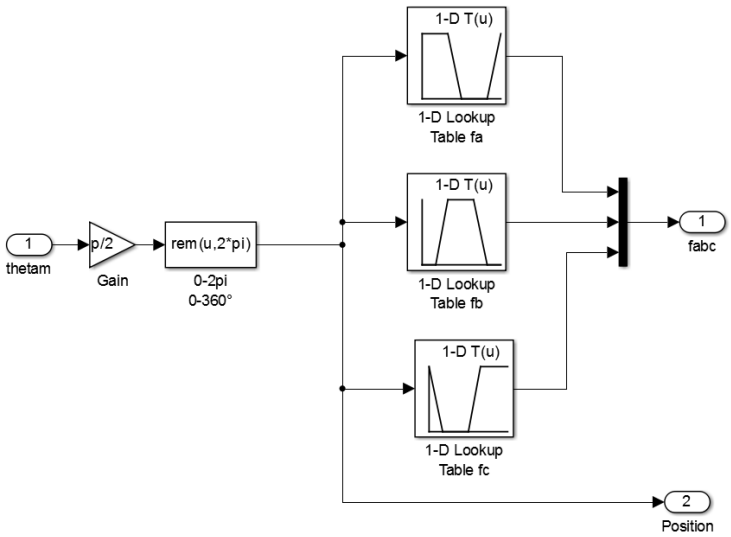

Figure 5.4: Trapezoidal back EMF functions implementation.

A zero-check of the currents and the back EMFs are transformed to the inverter, because the output voltages of the inverter has to be adjusted. The reason of the adjustment is that current peaks result when switching off and on a phase. These peaks can be seen in figure 5.5.

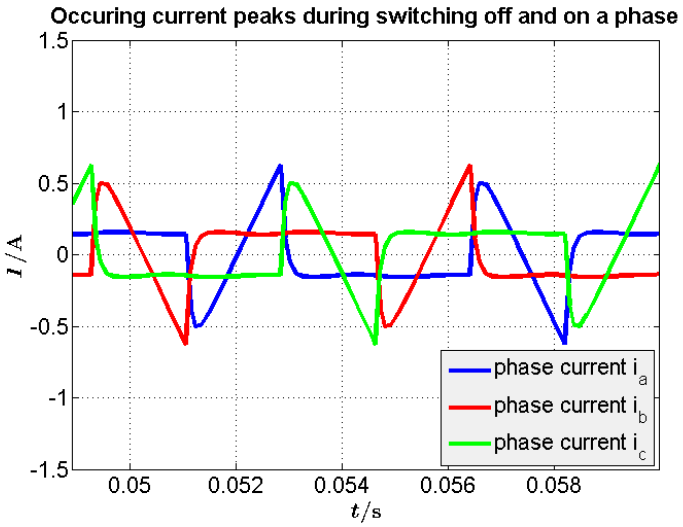

Figure 5.5: Current peaks during switching off and on a phase.

This does not happen for a real motor and inverter. The solution is that a voltage has to be considered, which replaces the freewheeling diode described in section 2.2.3. If a phase is switched off, the current flows through the freewheeling diode and the current of the turned on phase increases from zero. Additionally to the supply voltage the inverter has to consider the freewheeling diode current and prevent the peaks when switching off and on a phase. Table 5.2 shows the output voltages of the inverter considering the voltage of the freewheeling diode. [1]

The derivation of these voltages can be looked up in [1].

el. angle	diode	$\mathbf{V_{ab}}$	$\mathbf{V_{bc}}$	$\mathbf{V_{ca}}$
0° - 60°	$i_c \neq 0$	V_{DD}	0	-V_{DD}
	$i_c = 0$	V_{DD}	$\frac{1}{2}(-V_{DD} + e_a + e_b - 2e_c)$	$\frac{1}{2}(-V_{DD} - e_a + e_b + 2e_c)$
60° - 120°	$i_b \neq 0$	0	V_{DD}	-V_{DD}
	$i_b = 0$	$\frac{1}{2}(V_{DD} + e_a - 2e_b + e_c)$	$\frac{1}{2}(V_{DD} - e_a + 2e_b - e_c)$	-V_{DD}
120° - 180°	$i_a \neq 0$	-V_{DD}	V_{DD}	0
	$i_a = 0$	$\frac{1}{2}(-V_{DD} + 2e_a - e_b - e_c)$	V_{DD}	$\frac{1}{2}(-V_{DD} - 2e_a + e_b + e_c)$
180° - 240°	$i_c \neq 0$	-V_{DD}	0	V_{DD}
	$i_c = 0$	-V_{DD}	$\frac{1}{2}(V_{DD} + e_a + e_b - 2e_c)$	$\frac{1}{2}(V_{DD} - e_a + e_b + 2e_c)$
240° - 300°	$i_b \neq 0$	0	-V_{DD}	V_{DD}
	$i_b = 0$	$\frac{1}{2}(-V_{DD} + e_a - 2e_b + e_c)$	$\frac{1}{2}(-V_{DD} - e_a + 2e_b - e_c)$	V_{DD}
300° - 360°	$i_a \neq 0$	V_{DD}	-V_{DD}	0
	$i_a = 0$	$\frac{1}{2}(V_{DD} + 2e_a - e_b - e_c)$	-V_{DD}	$\frac{1}{2}(-V_{DD} - 2e_a + e_b + e_c)$

Table 5.2: Output voltages of inverter with implementation of freewheeling diode voltage. (modified from [1])

5.3 Mobile Robot Driving Simulation

For implementing the motion of the mobile robot equation (3.17) is used for the time optimal control and equation (3.16) is added to the state space equation (2.30) for the energy optimal control. At first, both control methods are tested on the simplified BLDC motor model of section 5.1. Secondly, the whole BLDC motor drive model of section 5.2 is controlled according to optimal time and optimal energy.

5.3.1 Mobile Robot Driving Simulation with simplified BLDC Motor Model

The motion behavior of the mobile robot is added to the simplified BLDC motor model. Afterwards, the position of the robot is controlled in optimal time and by consuming minimal energy.

Time Optimal Control of the Mobile Robot Position with simplified BLDC Motor Model

The time optimal control is implemented with a PID controller, where the controller output is limited to the rated voltage of the motor. The closed loop time optimal control of the position of the mobile robot is implemented like in figure 5.6. The red part includes the behavior of equation (3.18) with $C_d = 2 \cdot K_d \cdot v_0$. The green part calculates the power copper loss and measures the resulting energy loss. The energy loss is measured without the hill climbing force at first and then, this disturbance force is added.

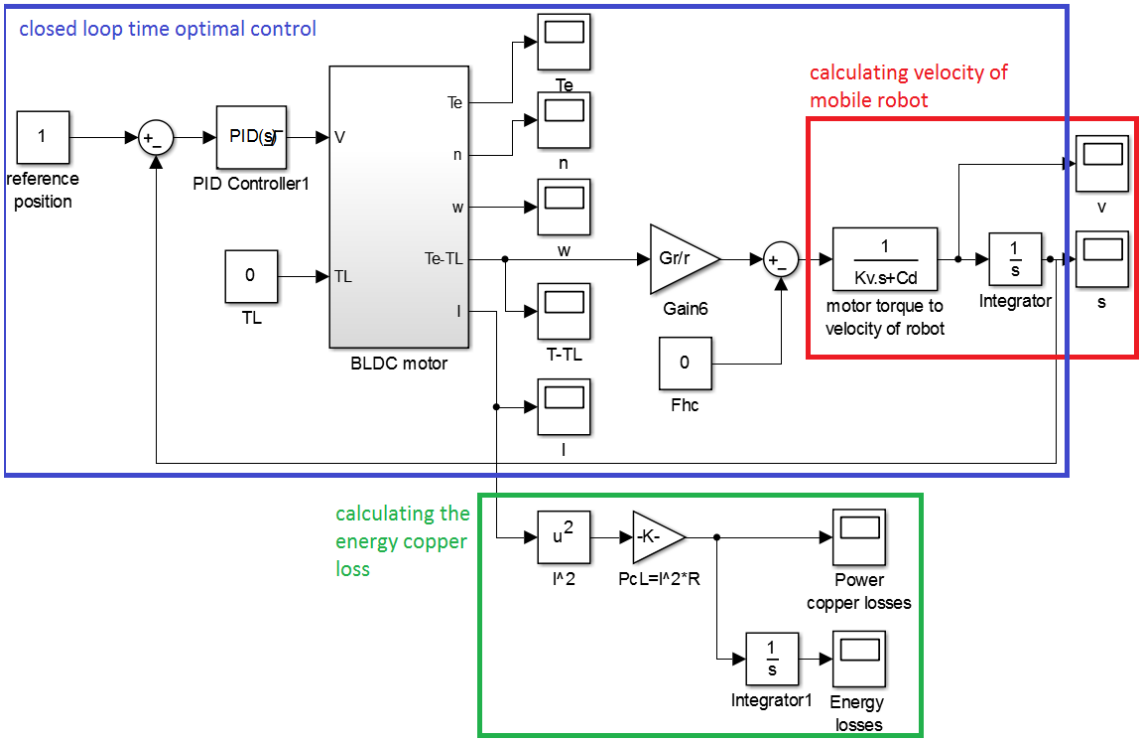

Figure 5.6: Time optimal position control of the mobile robot with the simplified BLDC motor model.

Energy Optimal Control of the Mobile Robot Position with simplified BLDC Motor Model

The optimal control theory about the LQR is applied for the energy optimal control. The simplified model in state space representation is needed for calculating the Kalman gain. Thus, the model is based on equation (2.30) and (3.16) including the hill climbing force, which leads to the equation

$$\begin{pmatrix} \dot{i} \\ \dot{\omega} \\ \dot{v} \\ \dot{s} \end{pmatrix} = \begin{pmatrix} -\frac{R}{L} & -\frac{k_e}{L} & 0 & 0 \\ \frac{k_T}{J} & -\frac{B_f}{J} & 0 & 0 \\ \frac{k_T \cdot G_r}{r \cdot K_v} & 0 & -\frac{C_d}{K_v} & 0 \\ 0 & 0 & 1 & 0 \end{pmatrix} \begin{pmatrix} i \\ \omega \\ v \\ s \end{pmatrix} + \begin{pmatrix} \frac{1}{L} \\ 0 \\ 0 \\ 0 \end{pmatrix} V_{DD} + \begin{pmatrix} 0 \\ -\frac{r}{G_r \cdot J} \\ -\frac{1}{K_v} \\ 0 \end{pmatrix} F_{hc}, \tag{5.1}$$

$$y = Cx = \begin{pmatrix} 0 & 0 & 0 & 1 \end{pmatrix} \begin{pmatrix} i \\ \omega \\ v \\ s \end{pmatrix}, \tag{5.2}$$

with $C_d = 2 \cdot K_d \cdot v_0$. The whole simulation model is shown in figure 5.7. The closed loop is implemented as linear quadratic integrator. The integrator gain can be adjusted to avoid overshoot of the position. The input voltage of the motor is limited to the rated voltage. The hill climbing force can be switched on and off.

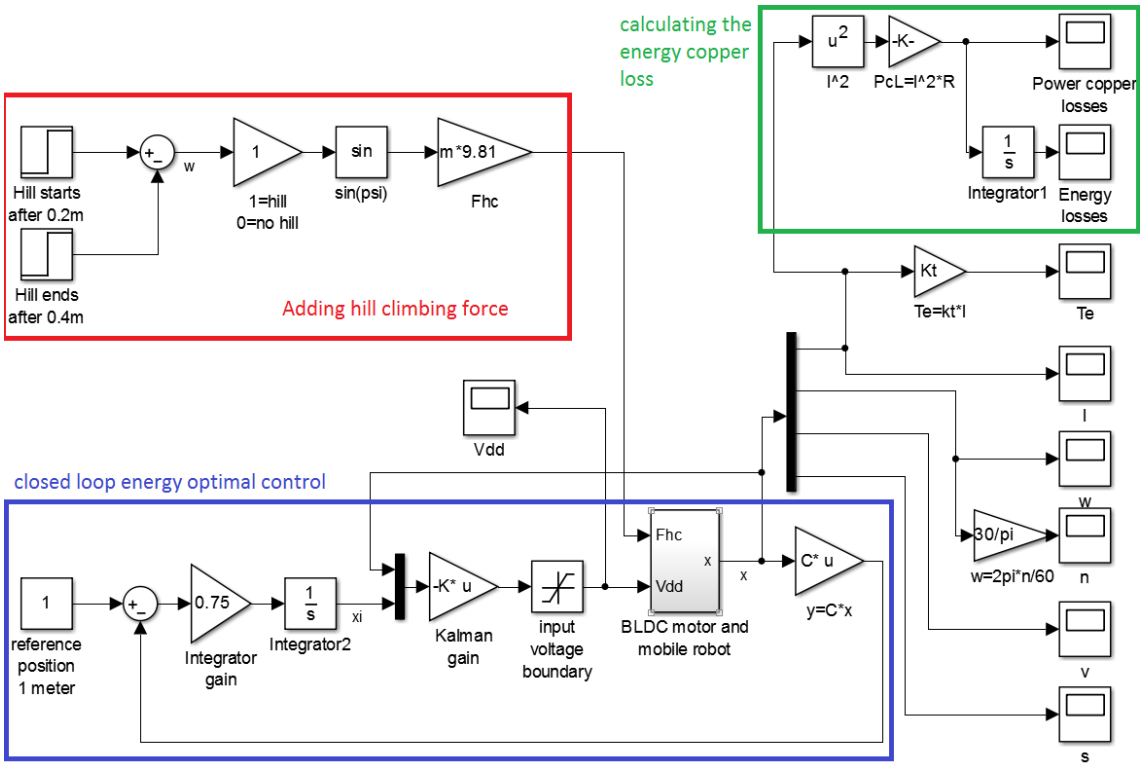

Figure 5.7: Energy optimal position control of the mobile robot with the simplified BLDC motor model.

5.3.2 Mobile Robot Driving Simulation with whole BLDC Motor Drive Model

The time and energy optimal control is applied to the whole BLDC motor drive model. This control scheme is a good approximation for the real system. The motion of the mobile robot is added to the model of section 5.2.

Time Optimal Control of the Mobile Robot Position with whole BLDC Motor Drive Model

A PID controller with the same parameters of equation (6.3) is used to regulate the supply voltage. The whole simulation is shown in figure 5.8. The energy copper losses can be calculated out of the torque and the torque constant k_T or the average current.

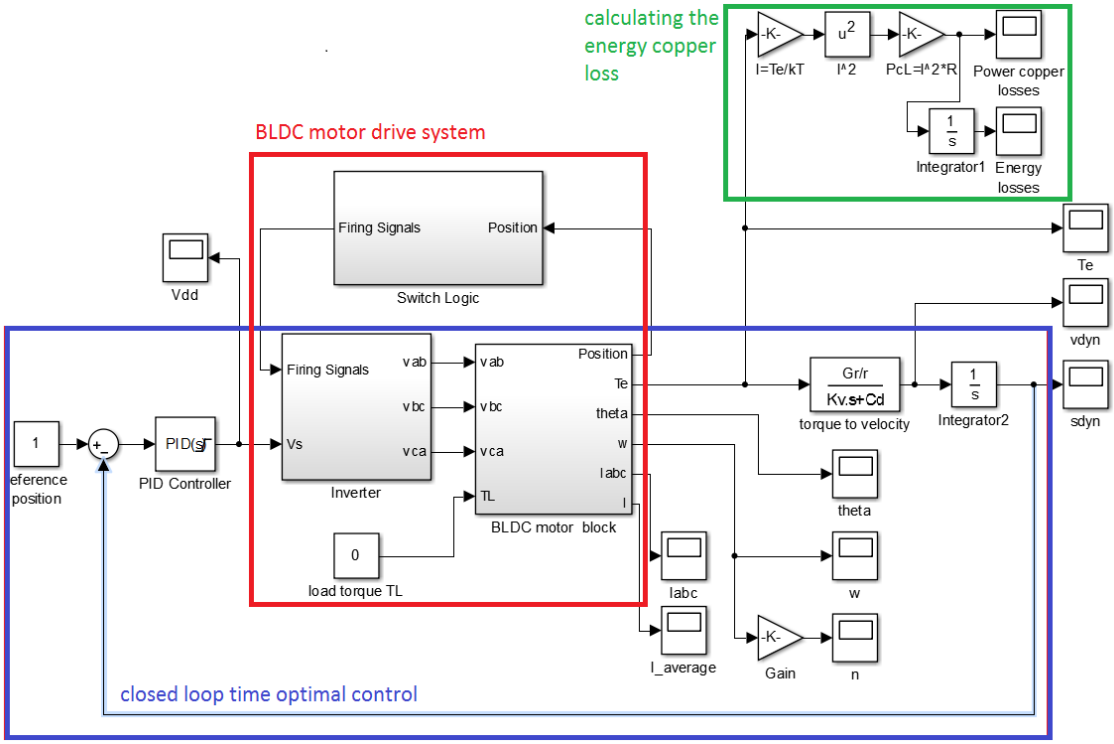

Figure 5.8: Time optimal position control of the mobile robot with the whole BLDC motor drive model.

Energy Optimal Control of the Mobile Robot Position with whole BLDC Motor Drive Model

The energy optimal control for the whole BLDC motor drive system is implemented as in figure 5.9. The Kalman gain is calculated with the state space equation (5.1) and the output y with equation (5.2). The reason is that the multiplication with the Kalman gain results in one voltage and not in the three line-to-line voltages of the BLDC motor. Thus, the state space equation (2.26) can not be used for calculating the Kalman gain, but is applied in the BLDC motor block. The average current $I_{average}$ is used as current state for the calculation of the Kalman gain.

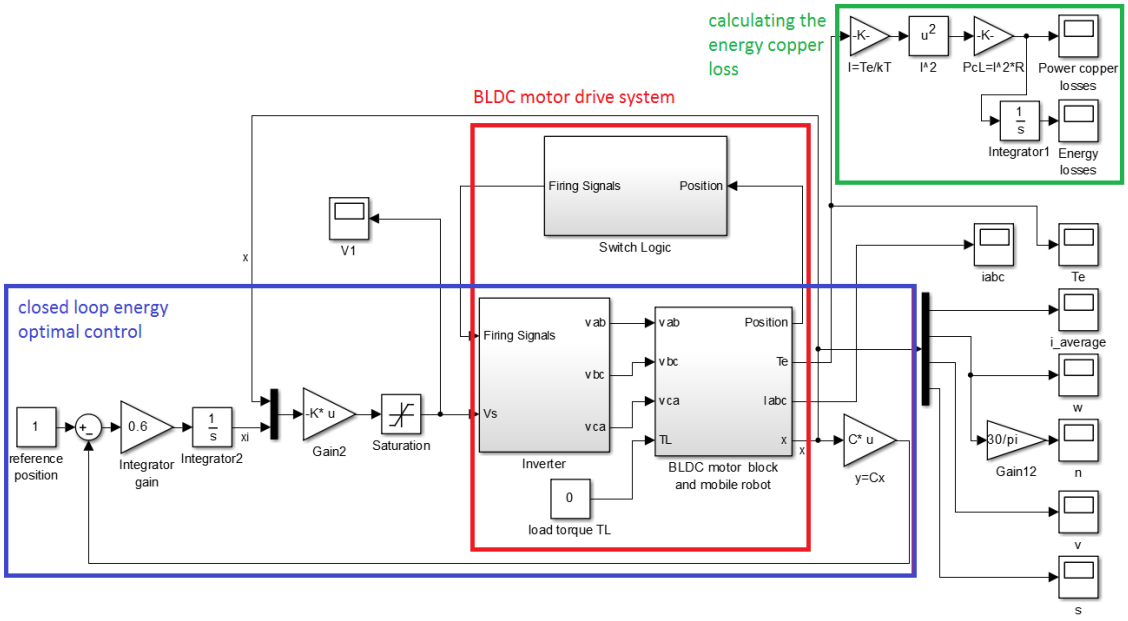

Figure 5.9: Energy optimal position control of the mobile robot with the swhole BLDC motor drive model.

6 Results

All results are presented in this chapter. This includes the step response of the simplified BLDC motor model and the whole BLDC motor drive model. These models are verified by creating the diagrams of rotational speed, current, mechanical power and efficiency over the torque, which are given from the data sheet. The step response of time and energy optimal control are explained. Finally, the energy savings due to energy optimal control are presented.

6.1 Step Response of the BLDC Motor Models

A step of the supply voltage is applied and the behavior of current, torque, back EMF and rotational speed is plotted. The BLDC motor DM1422-03 of Telco Motion [6] is chosen, because it is the smallest motor which has been found. Thus, this motor is appropriate for applications with small mobile robots. The data sheet provides the following values:

$$
\begin{aligned}
r_a &= 165\Omega, \\
L_a &= 0.15H, \\
V_{rate} &= 3V, \\
n_0 &= 780min^{-1}, \\
\omega_0 &= 81.68\frac{rad}{s}, \\
P_{out} &= 0.01W, \\
\eta_{max} &= 0.18, \\
I_0 &= 0.006A, \\
T_S &= 0.3mNm, \\
T_f &= 0.15mNm, \\
B_f &= 0.0000018364032\frac{Nm}{\frac{rad}{s}}, \\
J &= 0.000000012kgm^2, \\
k_e &= 0.024637\frac{V}{\frac{rad}{s}}, \\
k_T &= 0.02461\frac{Nm}{A}, \\
p &= 2,
\end{aligned}
$$

where

r_a is the phase-to-phase resistance,
L_a is the phase-to-phase inductance,
V_{rate} is the rated voltage,
n_0 is the no-load rotational speed,

ω_0 is the no-load angular speed,
P_{out} is the mechanical output power,
η_{max} is the maximal efficiency,
I_0 is the no-load current,
T_S is the stall torque,
T_f is the friction torque,
B_f is the viscous friction coefficient,
J is the moment of inertia,
k_e is the back EMF constant,
k_T is the torque constant and
p is the number of poles. [6]

The inductance L_a is assumed and the viscous friction coefficient is calculated with

$$B_f = \frac{T_f}{\omega_0}. \tag{6.1}$$

These values are applied to both the simplified BLDC motor model and the whole BLDC motor drive model and the step response is plotted.

6.1.1 Step Response of the simplified BLDC Motor Model

The step response shows the starting behavior of the simplified BLDC motor model of section 5.1. No load torque is applied and thus, $T_L = 0$. The torque behavior is shown in figure 6.1. It rises to the stall torque at beginning and decreases to the friction torque.

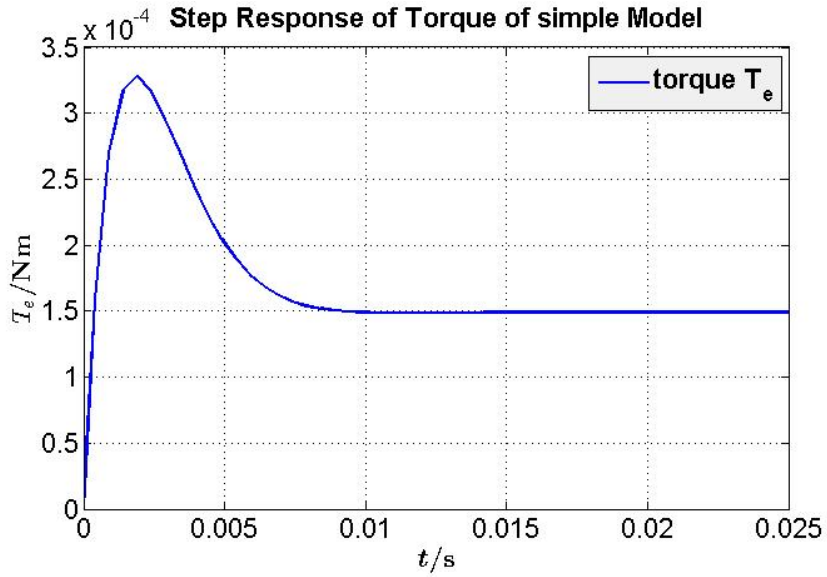

Figure 6.1: Step response of torque of the simplified BLDC motor model.

The current looks like the torque waveform. The difference is just the factor k_T. Figure 6.2 shows the current waveform over time of the simplified motor model. The current decreases to the no-load current I_0.

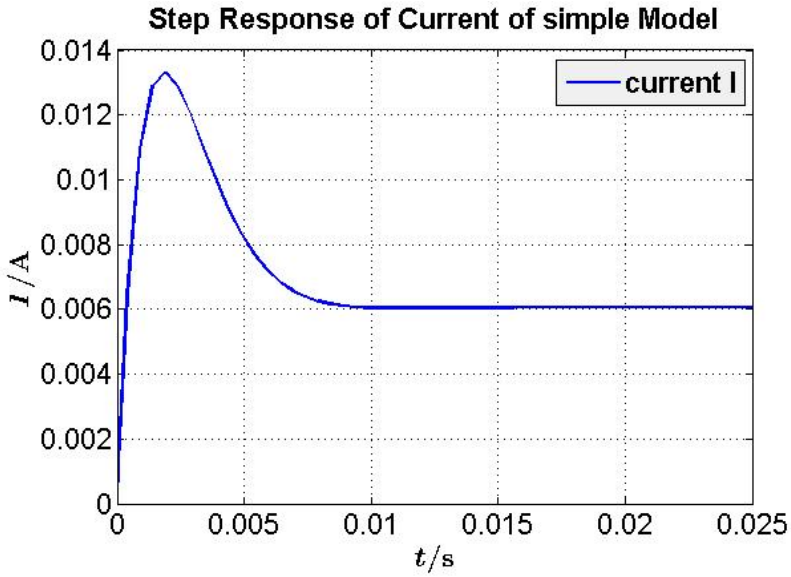

Figure 6.2: Step response of current of the simplified BLDC motor model.

The rotational speed starts from zero and increases to the no-load speed. The step response of the rotational speed is shown in figure 6.3.

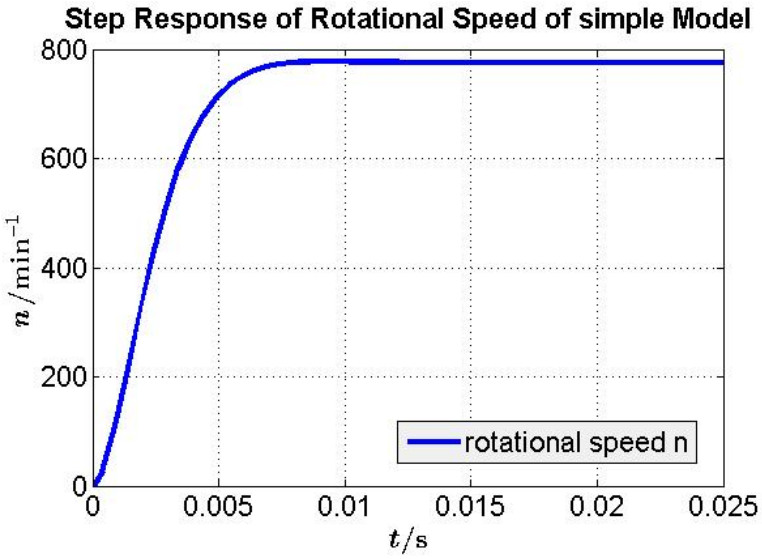

Figure 6.3: Step response of rotational speed of the simplified BLDC motor model.

The back EMF is proportional to the angular speed. The factor is the back EMF constant k_e for the simplified model. Figure 6.4 shows that the back EMF rises to 2V. If friction is not considered the back EMF would reach the supply voltage of 3V.

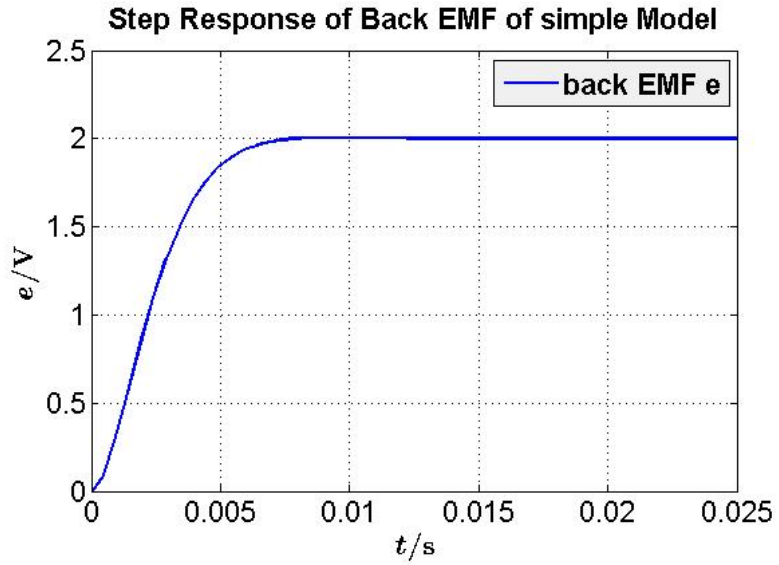

Figure 6.4: Step response of back EMF of the simplified BLDC motor model.

6.1.2 Step Response of the whole BLDC Motor Drive Model

The starting behavior of the whole BLDC motor drive model of section 5.2 is achieved with an applied step to the supply voltage V_{DD}. The same values are plotted as in the previous section. The torque has the same waveform than before, but ripples occur due to the switching sequence of the inverter. This can be seen in figure 6.5.

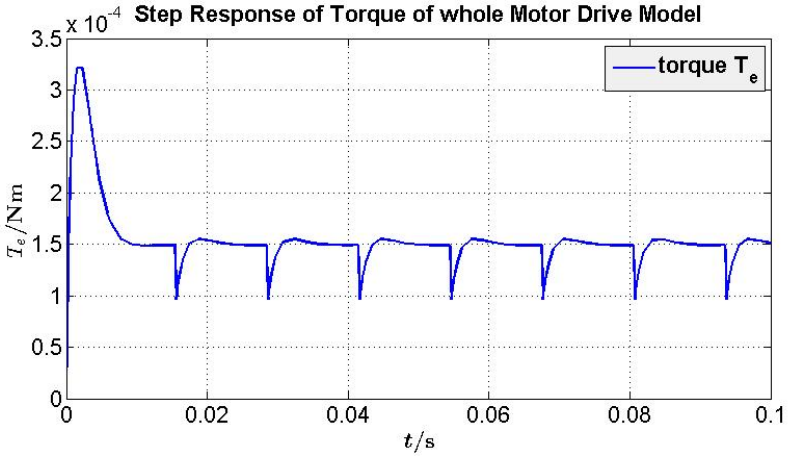

Figure 6.5: Step response of torque of the whole BLDC motor drive model.

The three phase currents have a similar waveform than in figure 2.4. Since switching off a phase is faster than switching on another phase, such ripples occur which results in quasi-square waveforms shown in figure 6.6.

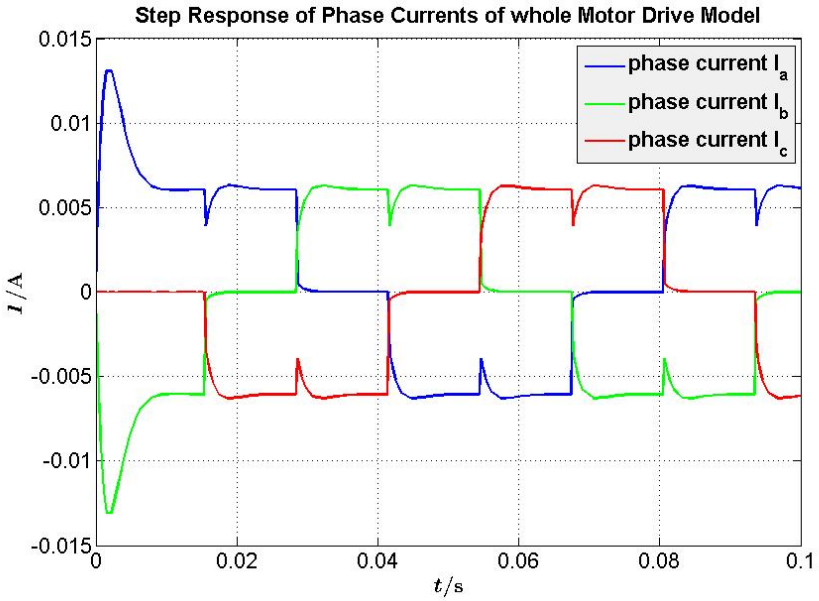

Figure 6.6: Step response of phase currents of the whole BLDC motor drive model.

The resulting rotational speed is similar to that of the previous section. The torque ripples are filtered due to the moment of inertia of the rotor. But in the case of such a small motor, small ripples of the rotational speed can remain. The behavior of the rotational speed is illustrated in figure 6.7

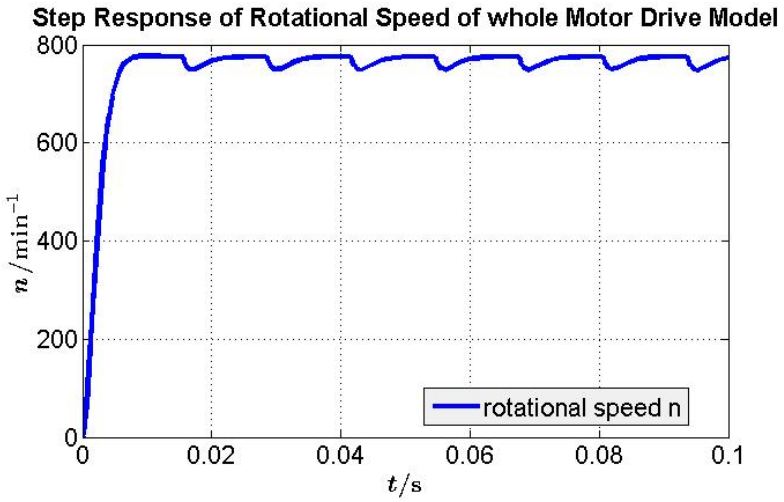

Figure 6.7: Step response of rotational speed of the whole BLDC motor drive model.

The rotor position equals the rotor angle, but starts from zero after 360° or 2π. Figure 6.8 shows the position, which is used by the switch logic to generate the switching sequence for the inverter.

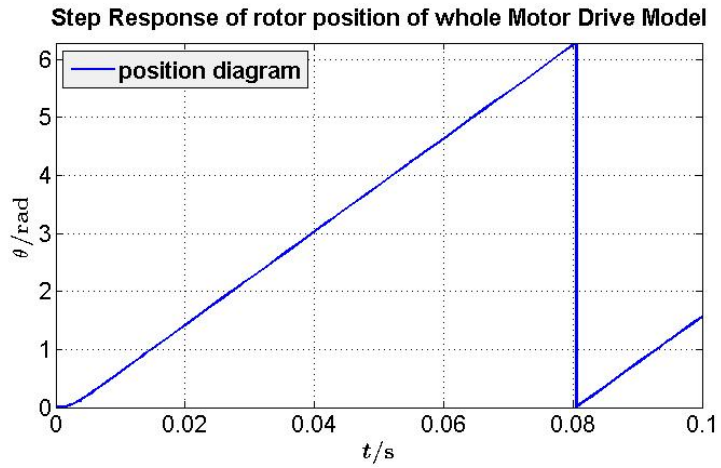

Figure 6.8: Step response of rotor position of the whole BLDC motor drive model.

The backs EMF have the trapezoidal waveform shown in figure 2.4. The step response of the back EMFs can be seen in figure 6.9.

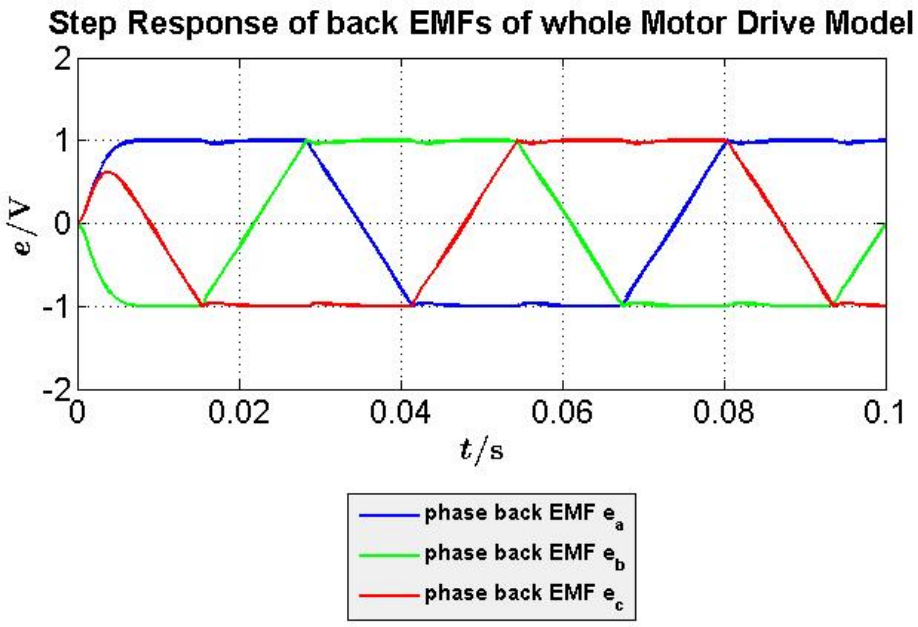

Figure 6.9: Step response of back EMFs of the whole BLDC motor drive model.

6.2 Verification of the BLDC Motor Models

The model is verified with the BLDC motor DM1428-10 of Telco Motion [6] because the data sheet of this motor provides all performance curves as comparison. The values for this motor are

$$
\begin{aligned}
r_a &= 3.6\Omega, \\
L_a &= 0.0003H, \\
V_{rate} &= 10V, \\
n_0 &= 21520min^{-1}, \\
P_{out} &= 4.44W, \\
\eta_{max} &= 0.6, \\
I_0 &= 0.14A, \\
T_S &= 11.11mNm, \\
T_f &= 0.59mNm, \\
B_f &= 0.000000261806923\frac{Nm}{\frac{rad}{s}}, \\
J &= 0.000000022kgm^2, \\
k_e &= 0.00420169\frac{V}{\frac{rad}{s}}, \\
k_T &= 0.00421\frac{Nm}{A}, \\
p &= 2. \text{ [6]}
\end{aligned}
$$

The performance curves of the data sheet are shown in figure 6.10. The rotational speed, current, output power and effiecency are plotted over the torque. The optimizing region provides the highest efficiency.

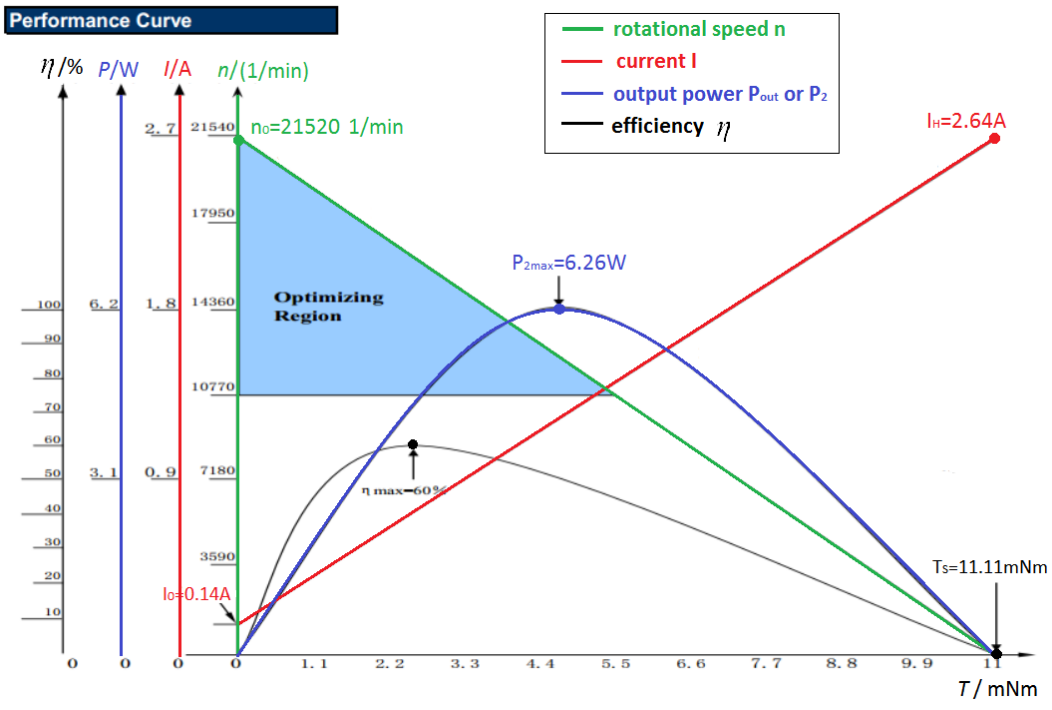

Figure 6.10: Performance curves from the data sheet of the BLDC motor. (modified from [6])

6.2.1 Verification of the simplified BLDC Motor Model

The rotational speed over the torque is similar to that of the data sheet. The n-T behavior of the data sheet is an ideal case, where the stall torque is reached in infinitesimal time. The comparison between ideal and measured behavior is shown in figure 6.11.

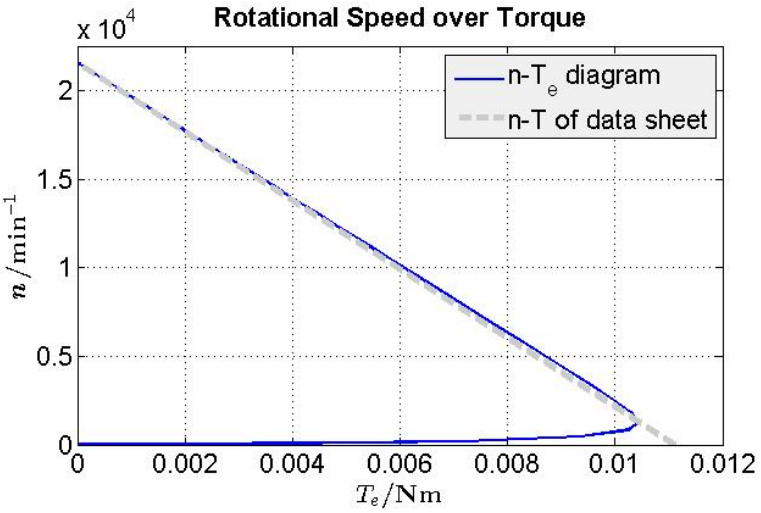

Figure 6.11: n-T diagram of the simplified BLDC motor model.

The current has the same waveform than the data sheet provides, as figure 6.12 shows. An approximation has been done because the no-load current in ideal case is at zero torque. But in practical case it is reached at the friction torque. So, the measured values are shifted so that the no-load current is reached at zero torque.

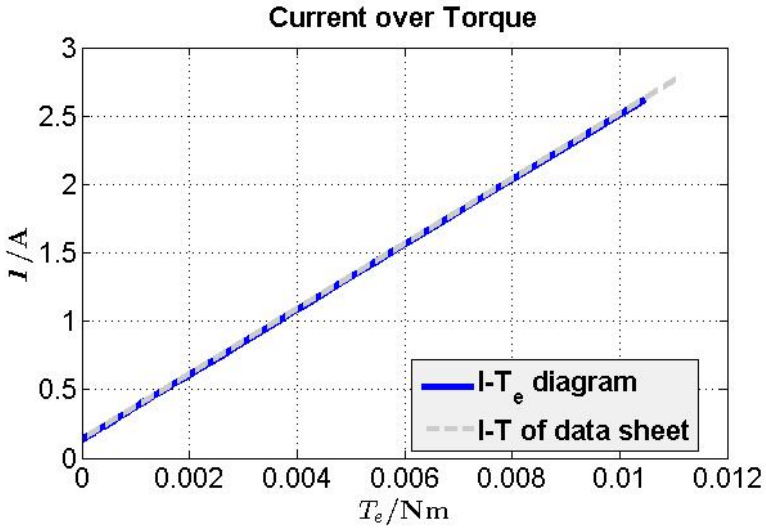

Figure 6.12: I-T diagram of the simplified BLDC motor model.

The power and efficiency plots are nearly the same than the waveforms of the data sheet. The peak values of both are a little bit higher than the ones of the performance curves. The reason can be that the mechanical output power of the data sheet is lower due to other losses than only the viscous friction. The power and efficiency over the torque are shown in figures 6.13 and 6.14.

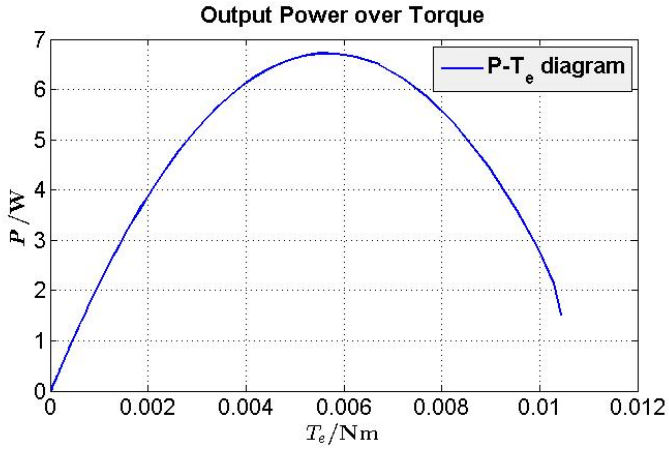

Figure 6.13: P-T diagram of the simplified BLDC motor model.

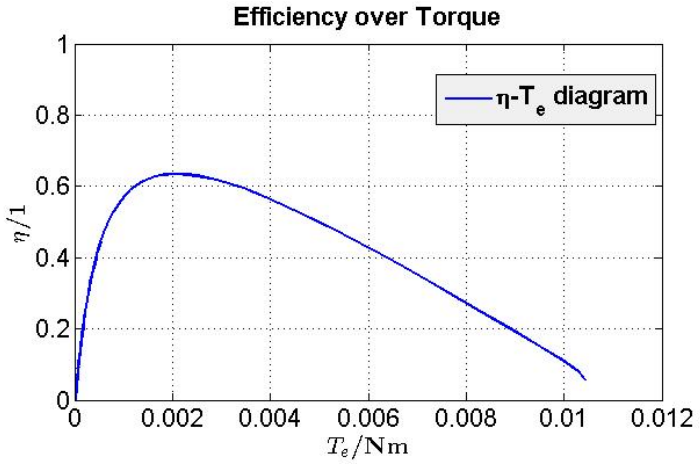

Figure 6.14: P-T diagram of the simplified BLDC motor model.

6.2.2 Verification of the whole BLDC Motor Drive Model

The behavior of the whole BLDC motor drive model is similar than the one of the previous section. The n-T diagram include the torque ripples as shown in figure 6.15.

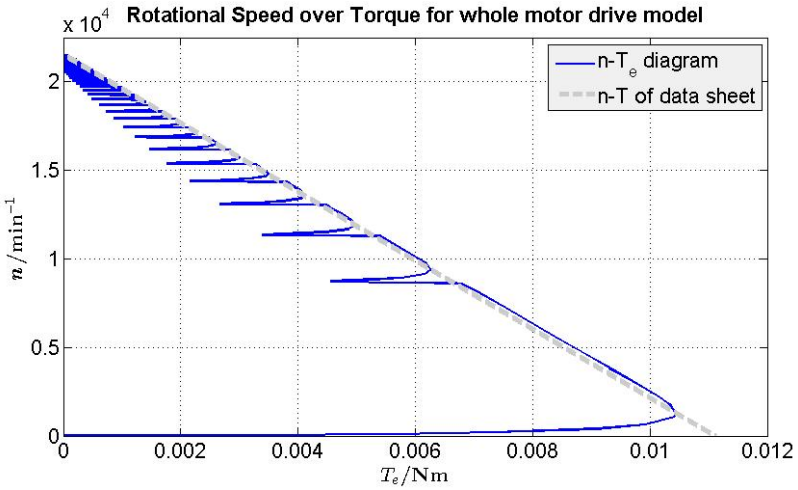

Figure 6.15: n-T diagram of the whole BLDC motor drive model.

To plot the current over torque the average current is used. The modulus of the three phase currents is added together and divided by 2 to obtain the average current. The same waveform than of previous section is achieved and is shown in figure 6.16.

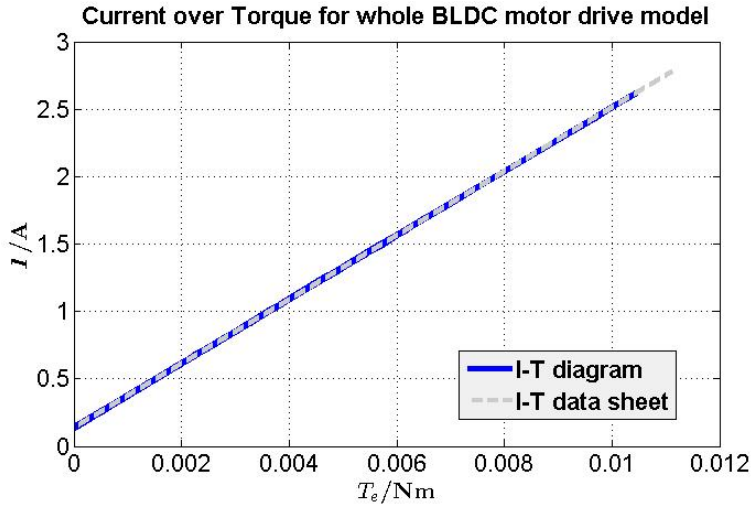

Figure 6.16: I-T diagram of the whole BLDC motor drive model.

The mechanical output power and efficiency diagram are affected by the torque ripples, which is shown in figures 6.17 and 6.18. Both waveforms still are similar to the ones provided from the data sheet.

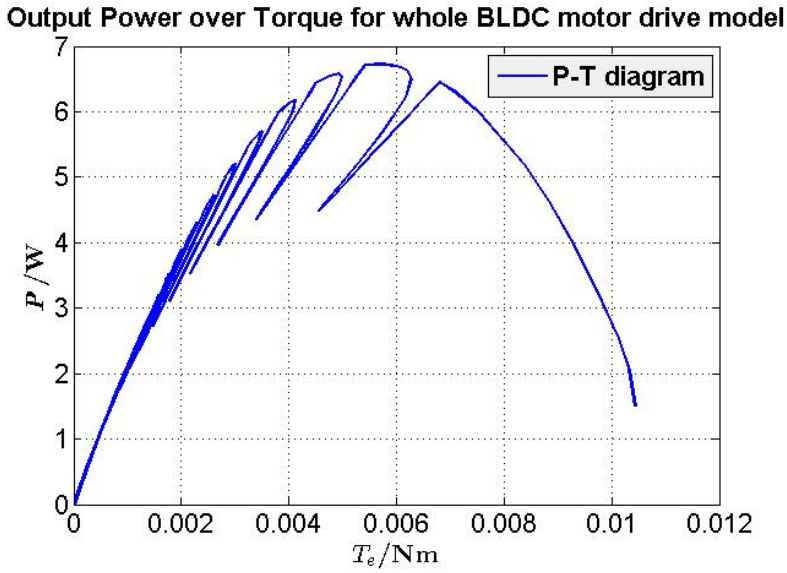

Figure 6.17: P-T diagram of the whole BLDC motor drive model.

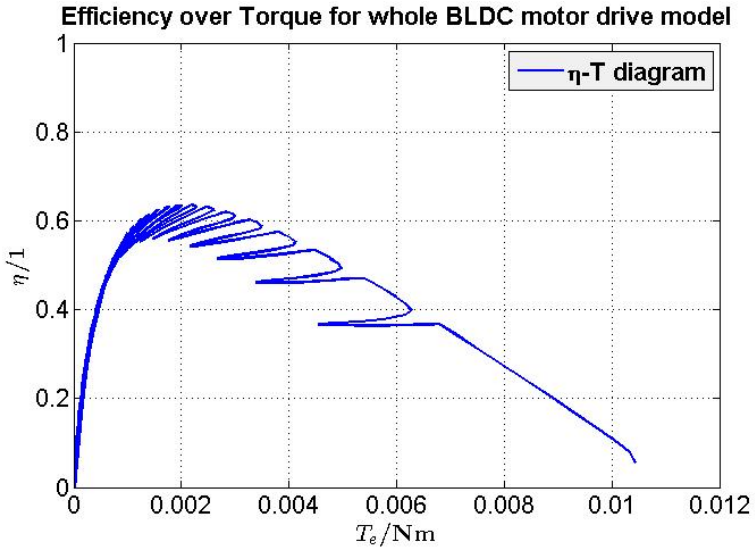

Figure 6.18: η-T diagram of the whole BLDC motor drive model.

6.3 Step Response of the Motion of the Mobile Robot

The step response of 1 meter of the reference position is the same for the simplified BLDC motor model and the whole BLDC motor drive model. Thus, it is just distinguished between time and energy optimal control. The missing parameters are assumed to be

$$\begin{aligned} K_v &= 0.1001kg, \\ C_d &= 0.5\frac{kg/s}{}, \\ G_r &= 1, \\ r &= 0.01m, \end{aligned}$$

where

K_v is a constant of the accelerating mass,
C_d is the overall constant due to drag,
G_r is the gear ratio between motor and tire and
r is the tire radius of the mobile robot.

6.3.1 Step Response of Time Optimal Control

The parameters for the PID controller are adjusted manually and equal

$$\begin{aligned} k_P &= 40, \\ k_I &= 5, \\ k_D &= 5. \end{aligned} \tag{6.2}$$

The reference position of 1 meter is reached after t=37s for the time optimal control loop. The step response of the position is shown in figure 6.19.

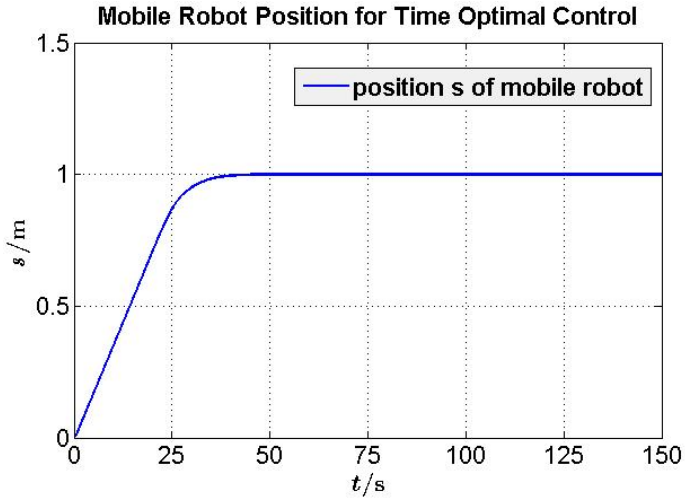

Figure 6.19: Position of the mobile robot for time optimal control.

The corresponding velocity of the mobile robot and input voltage to the BLDC motor are shown in figure 6.20 and 6.21.

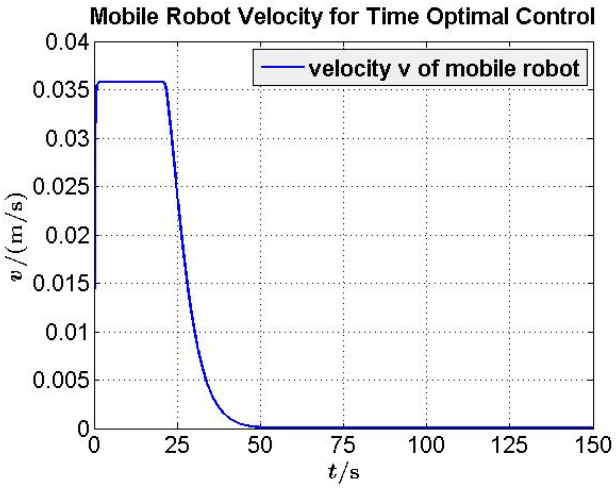

Figure 6.20: Velocity of the mobile robot for time optimal control.

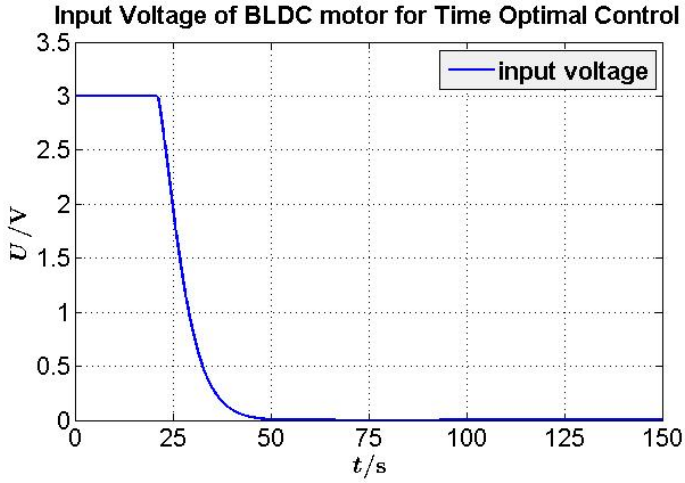

Figure 6.21: Input voltage of BLDC motor for time optimal control.

6.3.2 Step Response of Energy Optimal Control

The weighting matrix R is kept at 1 and the parameter q for the weighting matrix Q is adjusted. The matrix Q equals

$$Q = \begin{pmatrix} q & 0 & 0 & 0 & 0 \\ 0 & q & 0 & 0 & 0 \\ 0 & 0 & q & 0 & 0 \\ 0 & 0 & 0 & q & 0 \\ 0 & 0 & 0 & 0 & 1 \end{pmatrix}, \tag{6.3}$$

where the 1 is for the output value of the integrator and q weights the states x. The position waveform with q=0.01 is shown in figure 6.22. The final position of 1m is approached after t=80s.

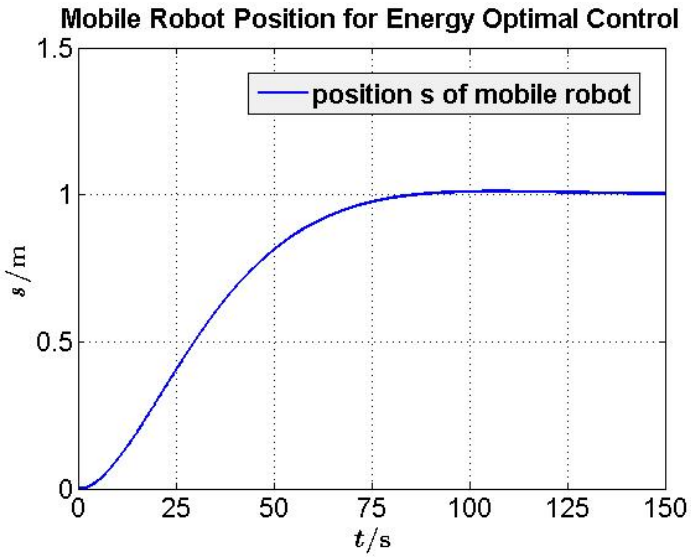

Figure 6.22: Position of the mobile robot for energy optimal control.

Figure 6.23 and 6.24 show the velocity of the mobile robot and the input voltage of the BLDC motor.

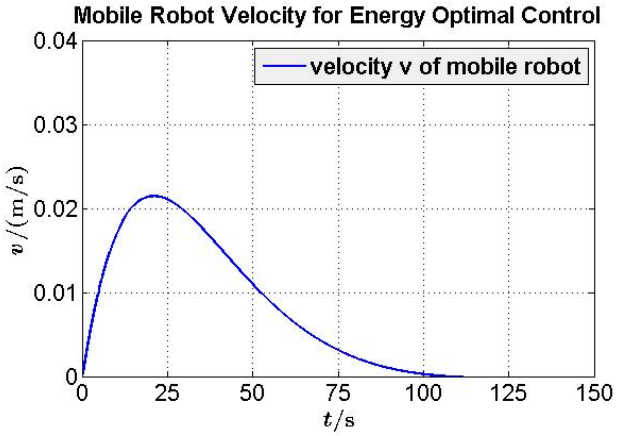

Figure 6.23: Velocity of the mobile robot for energy optimal control.

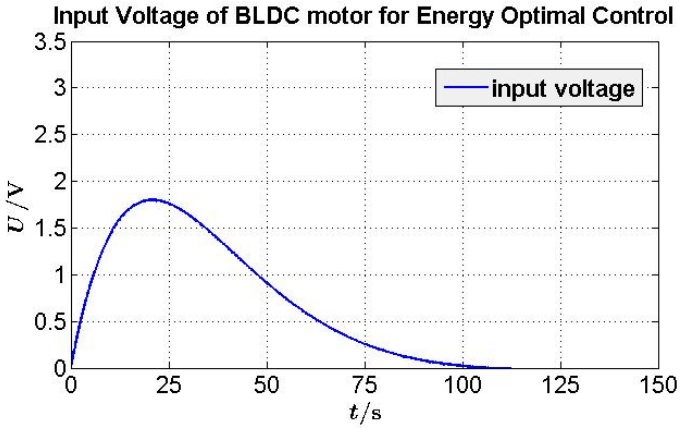

Figure 6.24: Input voltage of BLDC motor for energy optimal control.

6.4 Energy Savings due to Energy Optimal Control

The parameter q can be varied to achieve higher energy savings. The behavior of the energy loss over time is illustrated in figure 6.25. The time optimal control provide the fastest settling time, but the highest energy loss occurs. Choosing the parameter q is a tradeoff between energy loss and settling time. Between q=0.1 and q=1 less energy is saved as compared to the increasing settling time.

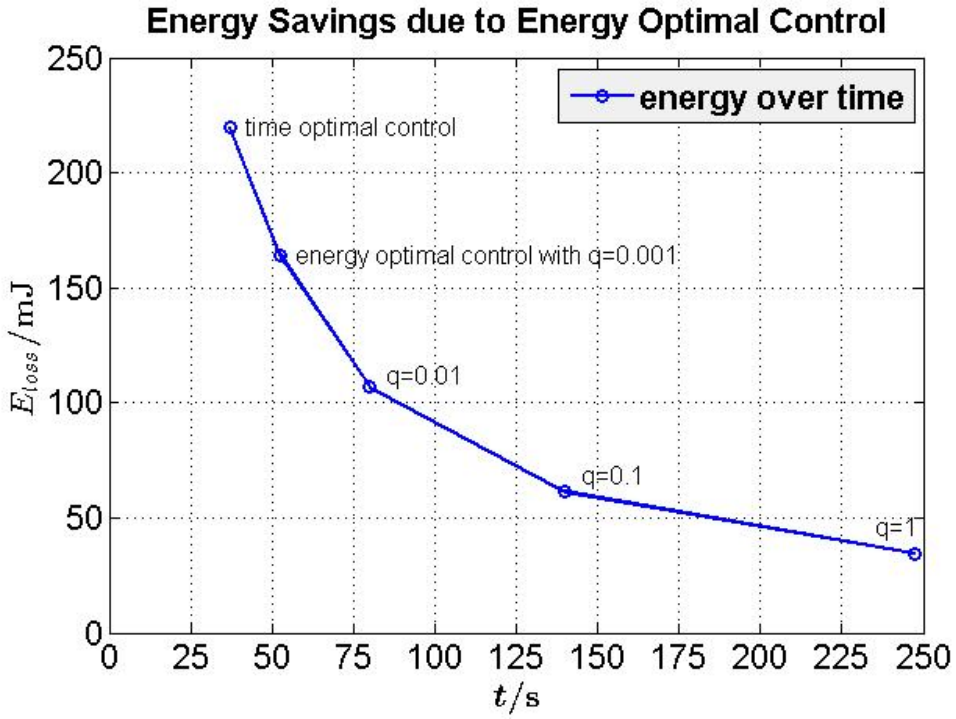

Figure 6.25: Energy savings due to energy optimal control.

7 Conclusion

It is concluded that energy consumption of mobile robots could be saved with appropriate motor control methods and thus, the operational time could be prolonged. This is important for the future of mobile robots. Therefore, the optimal control theory of the linear-quadratic-regulator provide a good opportunity to control linear models in state space representation. The gaining popularity and the limited energy capacity of mobile robots demand further study of reducing the energy consumption. The motors of mobile robots require the most energy and thus, appropriate control to decrease the motor losses obtain good results.

7.1 Summary

First, the driving principle and construction of BLDC motors are explained. The mathematical model and the losses of this motor are derived. Then, the tractive effort to accelerate the mobile robot is detailed. To get an overview of the objective of energy optimal control the difference of time and energy optimal control is specified. The PID controller is described, which is used for time optimal control. The optimal control theory and the linear-quadratic-regulator are explained, which is needed for energy optimal control. Three different control strategies, namely the hysteresis band control, the PWM control and the variable DC-link voltage control, are introduced. Afterwards, the BLDC motor model and the mobile robot motion are implemented in MATLAB®/SIMULINK®. Finally, the results of the models and the energy savings are presented.

7.2 Further Work

The performance curves of the real BLDC motor could be measured and compared with the motor model. The motor models could be improved by including drag of the rotor additional to the viscous friction. Furthermore, two or four BLDC motors could be considered to drive the tires of the mobile robot. The mobile robot could be constructed and time and energy optimal control could be applied on the real robot and the results could be compared. Thus, one of the control strategies must be implemented to regulate the input voltage of the BLDC motor. Additionally, more scenarios could be tested, for example to add the hill climbing force and measure the energy consumption for different road angles. Moreover, the rolling resistance of the tires could be considered. This method of reducing energy losses could be implemented for other types of robots like the micro unmanned aerial vehicle (micro UAV).

Bibliography

[1] S. Baldursson, "BLDC Motor Modelling and Control - A Matlab®/Simulink® Implementation," M.S. thesis, Dept. Elect. Power Eng., Chalmers Tekniska Högskola Institutionen för Energi och Miljö, Göteborg, Sweden, 2005.

[2] K. et al., "Simulation of Four Quadrant Operation & Speed Control of BLDC Motor on Matlab / Simulink," *International Journal of Science and Modern Engineering*, vol. 1, July 2013, [Online]. Available: http://www.ijisme.org/attachments/File/v1i8/H0373071813.pdf. [Accessed: Feb. 02, 2014].

[3] N. Matsui, "Sensorless PM Brushless DC Motor Drives," *IEEE Transactions on industrial Electronics*, vol. 43, no. 2, April 1996, [Online]. Available: IEEE Xplore, http://ieeexplore.ieee.org [Accessed: Feb. 05, 2014].

[4] P. Damodharan and K. Vasudevan, "Sensorless Brushless DC Motor Drive Based on the Zero-Crossing Detection of Back Electromotive Force (EMF) From the Line Voltage Difference," *IEEE Transactions on Energy Conversion*, vol. 25, no. 3, September 2010, [Online]. Available: IEEE Xplore, http://ieeexplore.ieee.org [Accessed: Feb. 07, 2014].

[5] F. K. et al., "Energy optimal motion control of servo motors and downsizing of components," in *Power Electronics and Applications, 2009. EPE '09. 13th European Conference*, Barcelona, 2009, pp. pp. 1–7.

[6] Telco Intercontinental Corp., "14mm brushless dc motor," Data Sheet, telco Motion. [Online]. Available: http://www.telcointercon.com/uploads/downloads/pdf/Brushless%20DC%20Motor/Micro%20bldc/DM14.pdf

[7] R. Krishnan, *Permanent Magnet Synchronous and Brushless DC Motor Drives*. CRC Press, 2010.

[8] C. Xia, *Permanent Magnet Brushless DC Motor Drives and Controls*. John Wiley & Sons Singapore Pte., Ltd., 2012.

[9] J. Larminie and J. Lowry, *Electric Vehicle Technology Explained*. John Wiley & Sons Singapore Pte. Ltd., 2003.

[10] M. Z. Haider, "Position Control of Permanent Magnet Brushless DC Motor using PID Controller," M.S. thesis, Dept. Elect. Instr. and Contr. Eng., Thapar University, Patiala, Punjab, India, 2011.

[11] Nanotec GmbH, "Stepper motor and bldc motors animation," May 21, 2014, [Sept. 26, 2012]. [Online]. Available: http://us.nanotec.com/support/tutorials/stepper-motor-and-bldc-motors-animation/

[12] P. Yedamale, "Brushless DC (BLDC) Motor Fundamentals," Microchip Technology Inc., Chandler, AZ, Application Note AN885, 2003.

[13] R. Schmitt. Newnes, 2002.

[14] J. Jezný and M. urilla, "Position Measurement with Hall Effect Sensors," *American Journal of Mechanical Engineering*, vol. 1, no. 7, pp. 149–195, 2013, [online]. Available: http://pubs.sciepub.com/ajme/1/7/16/. [Accessed: May 26, 2014].

[15] E. Hall, "On a New Action of the Magnet on Electric Currents," *American Journal of Mechanical Engineering*, vol. 2, no. 3, pp. 287–292, 1879, [online]. Available: http://www.jstor.org/stable/2369245?origin=JSTOR-pdf. [Accessed: May 26, 2014].

[16] A. P. C. Rao et al., "Mathematical Modeling of BLDC Motor wiht Closed Loop Speed Control using PID Controller under various Loading Conditions," *ARPN Journal of Engineering and Applied Sciences*, vol. 7, no. 10, Oct. 2012. [Online]. Available: http://www.arpnjournals.com/jeas/research_papers/rp_2012/jeas_1012_796.pdf

[17] The MathWorks Inc., "Linear-Quadratic-Gaussian (LQG) Design for Regulation," Help Function of MATLAB®.

[18] J. Zhong, "PID controller tuning: a short tutorial," 2006, Purdue University. [Online]. Available: http://saba.kntu.ac.ir/eecd/pcl/download/PIDtutorial.pdf

[19] R. Stärz, "Mess- und Steuerungstechnik 2," Script, Management Center Innsbruck.

[20] K. H. Ang et al., "PID Control System Analysis, Design, and Technology," *IEEE Transactions on Control Systems Technology*, vol. 13, no. 4, July 2005, [Online]. Available: IEEE Xplore, http://ieeexplore.ieee.org [Accessed: July. 15, 2014].

[21] F. L. Lewis et al., *Optimal Control, Third Edition*. John Wiley & Sons, Inc., 2012, pp. 19-176.

[22] D. E. Kirk, *Optimal Control, An Introduction*. Dover Publications, Inc., 2004, pp. 3-49.

[23] The MathWorks Inc., "Linear-Quadratic-Gaussian Control - lqi," Help Function of MATLAB®.

[24] M. e. a. Rahman, "Approaches to the control of torque and current in a brushless dc drive," in *Electrical Machines and Drives, 1993. Sixth International Conference on (Conf. Publ. No. 376)*, Sep. 1993, pp. 594–599.

[25] "Dsp solutions for bldc motors," TI Inc., Dallas, TX, Application Note BPRA055, Jan. 1997.

[26] Haitham Abu-Rub et al., *High Performance Control of AC Drives with MATLAB/Simulink Models*, first edition ed. John Wiley & Sons, Ltd., 2012, pp. 45-64.

[27] S. P. H. et al., "Two phase interleaved bidirectional dc-dc converter for electric vehicle using variable dc-link voltage," in *Vehicle Power and Propulsion Conference (VPPC), 2012 IEEE*, Oct 2012, pp. 748–752, [Online]. Available: IEEE Xplore, http://ieeexplore.ieee.org [Accessed: July. 18, 2014].

[28] B. Choi. Wiley-IEEE Press, 2013.

[29] K.-H. Kim and M.-J. Youn, "Performance comparison of PWM inverter and variable DC link inverter schemes for high-speed sensorless control of BLDC motor," *Electronics Letters*, vol. 38, no. 21, pp. 1294–1295, Oct. 2002, [Online]. Available: IEEE Xplore, http://ieeexplore.ieee.org [Accessed: July. 18, 2014].

List of Figures

List of Tables

List of Abbreviations

DC	direct current
BLDC motor	brushless direct current motor
PMBLDC motor	permanent magnet brushless direct current motor
PWM	pulse width modulation
back EMF	back electromotive force
PID controller	proportional-, integrative, derivative controller
PMSM	permanent magnet synchronous motor
AC	alternating current
IGBT	insulated bipolar gate transistor
P element	proportional element
I element	integral element
D element	derivative element
LQR	linear quadratic integrator
UAV	unmanned aerial vehicle